Gamma Gaussian Inverse Wishart Probability Hypothesis Density for Extended Target Tracking Using X-Band Marine Radar Data

Karl Granström, *Member, IEEE*, Antonio Natale, *Member, IEEE*, Paolo Braca, *Member, IEEE*, Giovanni Ludeno, *Member, IEEE*, and Francesco Serafino

***Abstract*—X-band marine radar systems represent a flexible and low-cost tool for the tracking of multiple targets in a given region of interest. Although suffering several sources of interference, e.g., the sea clutter, these systems can provide high-resolution measurements, both in space and time. Such features offer the opportunity to get accurate information not only about the target position/motion but also about the targets size. Accordingly, in this paper, we exploit emergent extended target tracking (ETT) methodologies in which the target state, typically position/velocity/acceleration, is augmented with the target length and width. In this paper, we propose an ETT procedure based on the popular probability hypothesis density filter, and in particular, we describe the extended target state through the gamma Gaussian inverse Wishart model. The comparative simplicity of the used models allows us to meet the real-time processing constraint required for the practical surveillance purposes. Real-world data from an experimental and operational campaign, collected during the recovery operations of the Costa Concordia wreckage in October 2013, are used to assess the performance of the proposed target tracking methodology. The full signal processing chain is implemented, and considerations of the experimental results are provided. Important nonideal effects, common to every marine radar, are observed and discussed in relation to the assumptions made for the tracking procedure.**

***Index Terms*—Extended target tracking (ETT), gamma Gaussian inverse Wishart-probability hypothesis density (GGIW-PHD), multiple target tracking (MTT), probability hypothesis density (PHD), random finite sets (RFSs), real-world experimental results, X-band marine radar.**

I. Introduction

X-BAND radars represent a useful tool for a number of civil and military applications, including weather and sea monitoring as well as air and maritime traffic control. Owing to their operative flexibility and ease of installation, these systems are suitable to scan the sea surface from fixed, moving, and—if need be—opportunity platforms.

In particular, X-band marine radars are largely employed for maritime surveillance purposes, i.e., to detect and track the targets occurring in a given scenario of interest. Moreover, the significant improvements gained in radar technologies in recent years allow us to get high-resolution radar data even from comparatively low-cost devices. Of course, these appealing features offer the opportunity to obtain more and more information about targets, thus increasing the performance of a marine surveillance system.

However, achieving the latter tasks requires the development of more sophisticated detection and tracking strategies with respect to the ones usually employed in a low-resolution framework. For instance, although the Gaussian model usually represents a proper means to describe the noise affecting traditional (i.e., low resolution) radar images, it is well recognized that, typically, such a model does not fit the spiky behavior of the sea clutter observed in high-resolution data. This assumption pushed the radar community to devise innovative detection schemes able to work in high-resolution scenarios; see, e.g., [1]–[6]. Nevertheless, the detection results provided by these techniques strongly depend on the sea conditions as well as on the radar quality and complexity. Therefore, the use of an effective multiple target tracking (MTT) system can play a fundamental role to improve the surveillance results, particularly when the remote monitoring of the sea surface is carried out through comparatively cheap devices.

Recall that a MTT system aims at tracking an unknown number of targets which appear and disappear at any time and at any location in the surveillance area. Popular approaches dealing with the MTT problem include the joint probabilistic data association (JPDA) filter [7], [8], the multiple hypothesis tracker (MHT) [7], and the probability hypothesis density (PHD) filter [9]. In particular, the PHD filters are gaining in popularity because they do not need to solve the computationally expensive data association problem [9], [10]. In addition to this attractive property, it can be shown that, by increasing the number of sensors, the multisensor PHD behaves as a mixture of as many Gaussian components as the true number of targets [11]–[13]. These Gaussian functions become progressively peakier around the true target states in a way that is ruled by the Fisher information [12]. In other words, the PHD is asymptotically optimal when the number of sensors increases.

However, traditional MTT techniques like JPDA and MHT were developed for low-resolution applications (see, e.g., [7]), where each target typically falls within a single resolution cell

Manuscript received October 3, 2014; revised January 26, 2015 and May 6, 2015; accepted May 30, 2015. The work of K. Granström was supported by the project Collaborative Unmanned Aircraft Systems funded by the Swedish Foundation for Strategic Research.

K. Granström was with Linköping University, 581 83 Linköping, Sweden. He is now with the Department of Electrical and Computer Engineering, University of Connecticut, Storrs, CT 06269 USA (e-mail: karl@engr.uconn.edu).

A. Natale, G. Ludeno, and F. Serafino are with the Istituto per il Rilevamento Elettromagnetico dell'Ambiente, Italian National Research Council (CNR), 80124 Napoli, Italy (e-mail: natale.a@irea.cnr.it; ludeno.g@irea.cnr.it; serafino.f@irea.cnr.it).

P. Braca is with NATO Science and Technology Organization, Centre for Maritime Research and Experimentation, 19126 La Spezia, Italy (e-mail: paolo.braca@cmre.nato.int).

Color versions of one or more of the figures in this paper are available online at http://ieeexplore.ieee.org.

Digital Object Identifier 10.1109/TGRS.2015.2444794

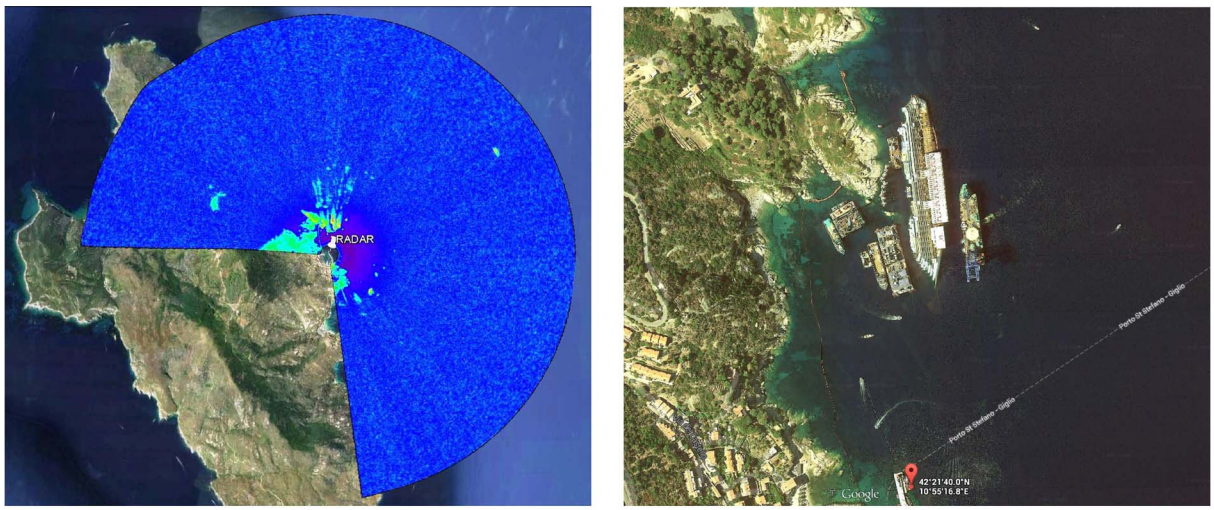

(a) (b)

Fig. 1. Location of data acquisition: Giglio Island on the coast of Tuscany, Italy. (a) Radar image overlaid on an optical image. (b) Detail of the acquisition site, close to the Costa Concordia wreckage. *Source*: 42°21′39.98″ N, 10°55′16.19″ E; *Google Earth*. Accessed March 13, 2012.

and therefore gives rise to, at most, a unique detection per radar scan. In such settings, the targets are usually denoted as *point* targets. Conversely, the high-resolution capabilities provided by modern radar systems make the typical targets occupy several resolution cells, i.e., each detected target can potentially give rise to multiple measurements per radar scan. In this case, the targets are denoted as *extended*, thus leading to the extended target tracking (ETT) problem; see, e.g., [7] and [14].

ETT problems can be approached by exploiting traditional MTT methods, provided that an intermediate clustering step is used to extract a representative sample (e.g., the barycenter) from each detection cloud [7]. However, this simplistic approach does not fully exploit all the information hidden in the available detection clouds because most of the targets' features (e.g., the shapes and sizes) are lost in the clustering step. Therefore, any attempt to retrieve both the kinematic and geometric properties of the targets should be treated using genuine ETT paradigms, which are able to work on the whole detection clusters.

In this paper, we present a novel multiple ETT system to obtain ETT estimates from raw high-resolution radar images. The core of the proposed system is a PHD filter which provides for each radar scan the kinematics (i.e., position, velocity, and turn rate), the size, and the shape, as well as the expected number of detections relevant to each target occurring in the surveillance area. The filter is fed with the measurements provided by a constant false alarm rate (CFAR) detector. As done in [15] and [16], the number of detections per radar scan is modeled with a Poisson distribution. However, here, we exploit a novel target appearance model to extend the results proposed in [17] to an ETT scenario. Furthermore, we devise an improved version of the random matrix detection model [18], [19] to take into account the errors introduced on the radar measurements by the polar to Cartesian coordinate conversion. The extended targets' states, i.e., the kinematic states together with the extension (size and shape) states of targets, are modeled by gamma Gaussian inverse Wishart (GGIW) distributions, thus leading to a new implementation of the extended target PHD filter proposed in [20]. The fully analytic implementation of the proposed tracking system represents a key feature to easily meet the real-time constraints of an actual surveillance system.

In order to test the GGIW-PHD filter, in this paper, we exploit the data collected in October 2013 by an incoherent X-band radar mounted at Giglio Island, in Italy, during the recovery operations of the Costa Concordia shipwreck [21]. A sample of the considered radar data, overlaid on an optical image of the experiment site, is shown in Fig. 1. Notice that, previously, ETT models have been applied to laser range data (see, e.g., [14] and [22]–[27]), Kinnect data (see, e.g., [28]), and video data (see, e.g., [29]). The track-before-detect of extended targets can be found in [30] and [31]. However, to the best of the authors' knowledge, this is the first time that an ETT algorithm has been applied to real radar data.

The experimental analysis demonstrates the capabilities of the proposed ETT strategy in dealing with cluttered measurements and with an unknown number of maneuvering targets, even if the estimates of the targets' shape suffer from the distortions introduced by the radar acquisition geometry, e.g., the shadowing phenomenon. Although the proposed measurement model mitigates some of these issues, innovative methods are still required to effectively handle the nonideality arising from the data acquisition process.

This paper is outlined as follows. A problem description is given in the next section, and the extended target model is presented in Section III. The GGIW-PHD filter is presented in Section IV, while the ETT results relevant to the considered radar data are presented in Section V, before the Conclusion.

II. Problem Formulation

During the data acquisition, a set of both stationary and moving targets was present in the surveillance area. The set of targets is denoted as

$$\mathbf{X}_k = \left\{ \xi_k^{(j)} \right\}_{j=1}^{N_{x,k}} \tag{1}$$

where k is the time step, $N_{x,k}$ is the number of targets present at that time step, and $\xi_k^{(j)}$ is the state of the jth target at that time step. Neither the true number of targets $N_{x,k}$ nor the target states $\xi_k^{(j)}$ are known, and they are therefore modeled as random variables. This nature of the problem—unknown number of targets with unknown states—makes it suitable to be approached

TABLE I
NOTATION

- $\mathbb{R}^n$ is the set of real n-vectors, $\mathbb{S}^n_+$ is the set of symmetric positive semi-definite $n \times n$-matrices, and $\mathbb{S}^n_{++}$ is the set of symmetric positive definite $n \times n$-matrices.
- $\mathbf{Z}_k = \left\{\mathbf{z}_k^{(j)}\right\}_{j=1}^{N_{z,k}}$ is a measurement set at time t_k, where $\mathbf{z}_k^{(j)} \in \mathbb{R}^{n_z}$, $\forall j$. $\mathbf{Z}^k$ denotes all measurement sets from time t_0 to time t_k.
- $V(\mathcal{A})$ is the volume of the surveillance area, $\lambda_k \triangleq \beta_{FA,k} V(\mathcal{A})$ is the mean number of clutter measurements and $c_k(\mathbf{z}_k) = 1/V(\mathcal{A})$ is the spatial distribution of the clutter over the surveillance volume.
- $\mathcal{P} \angle \mathbf{Z}$ denotes all the partitions $\mathcal{P}$ of the set $\mathbf{Z}$. A partition $\mathcal{P}$ is a set of non-empty subsets $\mathbf{W}$ called cells. The union of all cells $\mathbf{W}$ is equal to the set $\mathbf{Z}$. $|\mathbf{W}|$ represents the cardinality of a cell $\mathbf{W}$.
- For each cell $\mathbf{W}$ in each partition $\mathcal{P}$ the centroid measurement and scatter matrix are defined as

$$\bar{\mathbf{z}}_k^{\mathbf{W}} = \frac{1}{|\mathbf{W}|} \sum_{\mathbf{z}_k^{(i)} \in \mathbf{W}} \mathbf{z}_k^{(i)}, \; Z_k^{\mathbf{W}} = \sum_{\mathbf{z}_k^{(i)} \in \mathbf{W}} \left(\mathbf{z}_k^{(i)} - \bar{\mathbf{z}}_k^{\mathbf{W}}\right)\left(\mathbf{z}_k^{(i)} - \bar{\mathbf{z}}_k^{\mathbf{W}}\right)^{\mathrm{T}}.$$

- $f[g]$ denotes the integral $\int f(x)g(x)dx$.
- $\delta_{i,j}$ is the Kronecker delta, and $\otimes$ is the Kronecker product.
- $\mathbf{I}_n$ is a $n \times n$ identity matrix and $\mathbf{0}_{m \times n}$ is a $m \times n$ all zero matrix.
- $\mathrm{blkdiag}(A, B)$ is the block diagonalization of the matrices A and B.

using the random finite set (RFS) theory and PHD filters (see, e.g., [9] and [32]), which represent very powerful methods in dealing with multiple object estimation. A tutorial style introduction to random set methods, with applications to multiple extended object estimation, is given in [33]. The set of targets $\mathbf{X}_k$ is modeled as an RFS, i.e., a set with a random number of elements, where each element is a random variable.

An unlabeled target track $\mathcal{T}^{(j)}$ can be defined by a target appearance time step $t^{(j)}$, a target disappearance time step $s^{(j)} > t^{(j)}$, and a time sequence of target states $\xi_{t^{(j)}}^{(j)}, \xi_{t^{(j)}+1}^{(j)}, \ldots, \xi_{s^{(j)}-1}^{(j)}, \xi_{s^{(j)}}^{(j)}$, where $\xi_k^{(j)} \in \mathbf{X}_k$ for all $t^{(j)} \leq k \leq s^{(j)}$. The set of target tracks at time step k

$$\mathbf{T}_k = \left\{\mathcal{T}_k^{(j)}\right\}_{j=1}^{N_{t,k}} \tag{2}$$

is the set of target tracks $\mathcal{T}_k^{(j)}$ that currently exist ($t^{(j)} \leq k$ and $s^{(j)} \geq k$) in the surveillance area.

The problem considered in this paper is processing the radar data to obtain the estimates

$$\hat{\mathbf{T}}_{k|k} = \left\{\left(\hat{\mathcal{T}}_{k|k}^{(j)}, l_{k|k}^{(j)}\right)\right\}_{j=1}^{\hat{N}_{t,k|k}} \tag{3}$$

of the set of target tracks using a target labeling strategy $l_{k|k}^{(j)} \geq 1$; see more details in Section IV-C.

III. ETT MODELS

In this section, we present models for the extended target state, target motion, and detections. The used notation is presented in Table I, while the probability distributions exploited in this work are listed in Table II.

A. Extended Target State

The extended target state ξ_k is defined as the triple

$$\xi_k \triangleq (\gamma_k, \mathbf{x}_k, X_k). \tag{4}$$

Here, the random vector $\mathbf{x}_k = [\mathbf{p}_k, \; \mathbf{v}_k, \; \omega_k]^{\mathrm{T}} \in \mathbb{R}^5$ is the kinematic state, which describes the target's position $\mathbf{p}_k \in \mathbb{R}^2$, velocity $\mathbf{v}_k \in \mathbb{R}^2$, and turn rate $\omega_k \in \mathbb{R}^1$. The turn rate describes how the target's heading changes over time, i.e., how the direction of the velocity vector $\mathbf{v}_k$ changes. The random matrix $X_k \in \mathbb{S}^2_{++}$ is the extension state and describes the target's size and shape. Under the random matrix model [18], [19], the target shape is assumed to be an ellipse. The random matrix model is chosen to describe the extended target shape because it is a good combination of an informative shape model and low computational complexity. Finally, the random variable $\gamma_k > 0$ is the measurement rate that describes how many measurements the target, on average, generates per time step. In this paper, following [15] and [16], the number of target generated measurements is assumed to be Poisson distributed, and γ_k is in this case the Poisson rate.

TABLE II
PROBABILITY DISTRIBUTIONS

- $\mathcal{PS}(n;\, \gamma)$ denotes a Poisson probability mass function (pmf) defined overs the integer $n \in \mathbb{N}$ with rate parameter $\gamma > 0$,

$$\mathcal{PS}(n;\, \gamma) = \gamma^n e^{-\gamma} (n!)^{-1}.$$

- $\mathcal{G}(\gamma\,;\, \alpha, \beta)$ denotes a gamma probability density function (pdf) defined over the scalar $\gamma > 0$ with scalar shape parameter $\alpha > 0$ and scalar inverse scale parameter $\beta > 0$,

$$\mathcal{G}(\gamma\,;\, \alpha, \beta) = \beta^{\alpha} \Gamma(\alpha)^{-1} \gamma^{\alpha-1} e^{-\beta\gamma},$$

where $\Gamma(\cdot)$ is the gamma function. The expected value of γ is α/β.
- $\mathcal{N}(x\,;\, m, P)$ denotes the pdf of a Gaussian distribution defined over the vector x, with expected value vector $m \in \mathbb{R}^n$ and covariance matrix $P \in \mathbb{S}^n_+$.
- $\mathcal{IW}_d(X\,;\, v, V)$ denotes an inverse Wishart pdf defined over the matrix $X \in \mathbb{S}^d_{++}$ with scalar degrees of freedom $v > 2d$ and parameter matrix $V \in \mathbb{S}^d_{++}$, [34, Definition 3.4.1]

$$\mathcal{IW}_d(X\,;\, v, V) = \frac{2^{-\frac{v-d-1}{2}} \det(V)^{\frac{v-d-1}{2}}}{\Gamma_d\left(\frac{v-d-1}{2}\right) \det(X)^{\frac{v}{2}}} \operatorname{etr}\left(-\frac{1}{2} X^{-1} V\right),$$

where $\operatorname{etr}(\cdot) = \exp(\operatorname{Tr}(\cdot))$ represents the exponential of the matrix trace, and $\Gamma_d(\cdot)$ is the multivariate gamma function. The multivariate gamma function $\Gamma_d(\cdot)$ can be expressed as a product of the ordinary gamma function $\Gamma(\cdot)$, see [34, Theorem 1.4.1]. The expected value of X is $V/(v - 2d - 2)$.
- $\mathcal{W}_d(X\,;\, w, W)$ denotes a Wishart pdf defined over the matrix $X \in \mathbb{S}^d_{++}$ with scalar degrees of freedom $w \geq d$ and parameter matrix $W \in \mathbb{S}^d_{++}$, [34, Definition 3.2.1]

$$\mathcal{W}_d(X\,;\, w, W) = \frac{2^{-\frac{wd}{2}} \det(X)^{\frac{w-d-1}{2}}}{\Gamma_d\left(\frac{w}{2}\right) \det(W)^{\frac{w}{2}}} \operatorname{etr}\left(-\frac{1}{2} W^{-1} X\right).$$

The expected value of X is wW.

Conditioned on a history of previous measurement sets, denoted as $\mathbf{Z}^k$, the extended target state ξ_k is modeled as a GGIW distribution [19], [35]

$$\begin{aligned} p\left(\xi_k|\mathbf{Z}^k\right) &= p\left(\gamma_k|\mathbf{Z}^k\right) p\left(\mathbf{x}_k|\mathbf{Z}^k\right) p\left(X_k|\mathbf{Z}^k\right) && \text{(6a)} \\ &= \mathcal{G}(\gamma_k; \alpha_{k|k}, \beta_{k|k}) \mathcal{N}(\mathbf{x}_k; m_{k|k}, P_{k|k}) \\ &\quad \times \mathcal{IW}_d(X_k; v_{k|k}, V_{k|k}). && \text{(6b)} \end{aligned}$$

The gamma distribution is the conjugate prior for the Poisson rate, and the Gaussian-inverse Wishart distributions are the conjugate priors for Gaussian distributed radar detections (see further in Section III-C). We also use the shorthand notation

$$p\left(\xi_k|\mathbf{Z}^k\right) = \mathcal{GGIW}(\xi_k; \zeta_{k|k}) \tag{7}$$

where $\zeta_{k|k} = \{\alpha_{k|k}, \beta_{k|k}, m_{k|k}, P_{k|k}, v_{k|k}, V_{k|k}\}$ is the set of GGIW density parameters; see Table II.

Note that (6) models the measurement rate as independent of the kinematic and extension states. In reality, the number of

measurements that a target generates is typically dependent on the size of the target and the distance between the target and the sensor (i.e., it is dependent on the target's position), where a larger and/or closer target typically generates more measurements compared to a smaller and/or more distant target. However, modeling this dependence is not easy in the general case, and it has been shown in simulations that the assumption does not restrict the estimation performance; see, e.g., [35] and [36].

Furthermore, note that (6) models the kinematic state $\mathbf{x}_k$ and the extension state X_k as independent. These quantities can be modeled as dependent [18]; however, previous works (see, e.g., [19] and [37]) have shown that, by relaxing this dependence, the model (6) allows for a more general class of kinematic state vectors. For example, this assumption allows us to include the nonlinear turn rate in the kinematic vector. With a more general state vector, the process modeling is improved without any sacrifice in estimation performance [37]. The time update and the measurement update that are used here (see Sections IV-A and B) provide for the necessary interdependence between the estimates of $\mathbf{x}_k$ and X_k.

B. Dynamic Motion Models

The dynamic motion models describe how the extended target state evolves over time, i.e., they describe the transition from ξ_k to ξ_{k+1}. All targets that are present in the surveillance area are assumed to follow the same dynamic motion models. Furthermore, it is assumed that each target evolves over time independently of all other targets. Both of these assumptions are standard in MTT [7]. For longer discussions on extended target dynamics modeling, see, e.g., [18], [19], and [37].

1) Kinematic State: For the kinematics state, the motion model is

$$\mathbf{x}_{k+1} = \mathbf{f}(\mathbf{x}_k) + \mathbf{w}_k \tag{8}$$

where $\mathbf{w}_k$ is Gaussian process noise with zero mean and covariance $\mathbf{Q}$. The motion model $\mathbf{f}(\cdot)$ and process noise covariance $\mathbf{Q}$ are

$$\mathbf{f}(\mathbf{x}_k) = \begin{bmatrix} 1 & 0 & \frac{\sin(\omega_k T_s)}{\omega_k} & \frac{-1+\cos(\omega_k T_s)}{\omega_k} & 0 \\ 0 & 1 & \frac{1-\cos(\omega_k T_s)}{\omega_k} & \frac{\sin(\omega_k T_s)}{\omega_k} & 0 \\ 0 & 0 & \cos(\omega_k T_s) & -\sin(\omega_k T_s) & 0 \\ 0 & 0 & \sin(\omega_k T_s) & \cos(\omega_k T_s) & 0 \\ 0 & 0 & 0 & 0 & 1 \end{bmatrix} \mathbf{x}_k \tag{9a}$$

$$\mathbf{Q} = \mathbf{G} \begin{bmatrix} \sigma_a^2 & 0 & 0 \\ 0 & \sigma_a^2 & 0 \\ 0 & 0 & \sigma_\omega^2 \end{bmatrix} \mathbf{G}^{\mathrm{T}}, \quad \mathbf{G} = \begin{bmatrix} \frac{T_s^2}{2}\mathbf{I}_2 & \mathbf{0}_{2\times 1} \\ T_s \mathbf{I}_2 & \mathbf{0}_{2\times 1} \\ \mathbf{0}_{1\times 2} & T_s \end{bmatrix} \tag{9b}$$

where T_s is the sampling time, σ_a is the acceleration standard deviation, and σ_ω is the turn-rate standard deviation. This gives a Gaussian transition density

$$p(\mathbf{x}_{k+1}|\mathbf{x}_k) = \mathcal{N}(\mathbf{x}_{k+1}; \mathbf{f}(\mathbf{x}_k), \mathbf{Q}). \tag{10}$$

2) Extension State: For the extension state, the motion model is

$$X_{k+1} = M(\mathbf{x}_k) X_k M(\mathbf{x}_k)^{\mathrm{T}} \tag{11a}$$

$$M(\mathbf{x}_k) = \begin{bmatrix} \cos(\omega_k T_s) & -\sin(\omega_k T_s) \\ \sin(\omega_k T_s) & \cos(\omega_k T_s) \end{bmatrix}. \tag{11b}$$

This means that the extension is rotated by ω_k radians per second, i.e., the shape of the target rotates when the target is turning. The transition density is Wishart [37]

$$p(X_{k+1}|\mathbf{x}_k, X_k) = \mathcal{W}\left(X_{k+1}; n, n^{-1} M(\mathbf{x}_k) X_k M(\mathbf{x}_k)^{\mathrm{T}}\right) \tag{12}$$

where the scalar parameter n rules the uncertainty of the transition—the higher n is, the more certain the transition (12) is [37].

3) Measurement Rate: The measurement rate is assumed to be approximately constant over time

$$\gamma_{k+1} = \gamma_k. \tag{13}$$

An explicit transition density is not used; instead, the expected value is kept constant, and the variance is increased by multiplying with a factor $\eta_k > 1$. The closer η_k is to 1, the more certain the time evolution.

As stated in Section III-A, the measurement rates typically depend on both the size of the target and its distance from the sensor (i.e., depends on the position), and the model (13) neglects such dependences. However, constructing a general model for these dependences is very difficult, and the assumption simplifies further analysis significantly. Furthermore, as shown in [35], keeping the expected values constant and using the parameter η_k to increase the variances of the estimated measurement rates are sufficient to capture the variations over time.

C. Measurement Model

The raw radar data are processed by an order statistic-CFAR (OS-CFAR) detector (see Section V-B) that provides detections in polar coordinates, i.e., in the range (r)–azimuth (φ) plane. Following standard models [38], we assume that each polar radar detection is affected by independent zero mean Gaussian measurement noises, with the range and azimuth standard deviations equal to σ_r and σ_φ, respectively. The polar detections are converted into Cartesian detections using the standard conversion [38]

$$\mathbf{z}_k^{(j)} = \left[r_k^{(j)} \cos\left(\varphi_k^{(j)}\right), \quad r_k^{(j)} \sin\left(\varphi_k^{(j)}\right) \right]^{\mathrm{T}} \tag{14}$$

where $r_k^{(j)}$ and $\varphi_k^{(j)}$ are the range and azimuth coordinates of the jth detected sample at time step k and $\mathbf{z}_k^{(j)}$ is the Cartesian detection. Each detection is treated independently of the other detections. This way, in our conversion strategy, the Cartesian detections are not affected by errors caused by the interpolation and resampling procedures that are otherwise commonly used. Moreover, due to the polar to Cartesian conversion, the Gaussian noise covariance matrix in Cartesian coordinates becomes a function of range—the along-range variance is constant but the across-range variance increases as the range increases. This effect is taken into account in the target detection model presented hereinafter.

In the data, there are two types of detections: clutter detections (false alarms) and detections generated by targets that are present in the surveillance area. Thus, the set of detections is the

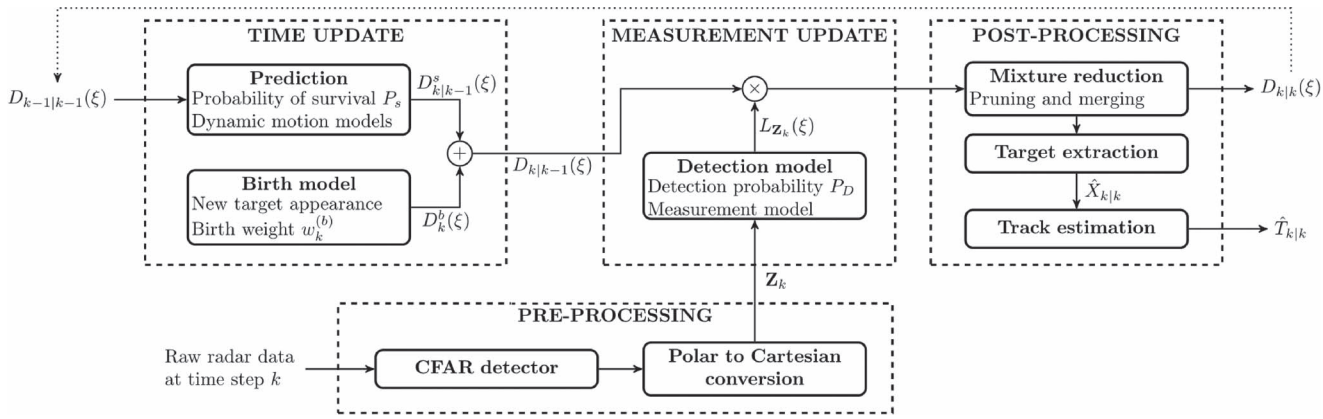

Fig. 2. Flowchart showing the essential parts of the employed target tracking system. In the preprocessing step, the raw radar data are first processed by a CFAR detector (see Section V-B) and then converted from polar to Cartesian coordinates. The GGIW-PHD filter is composed by three main blocks: the time update (see Section IV-A), the measurement update (see Section IV-B), and the postprocessing (see Section IV-C).

union of a set of clutter detections and a set of target generated detections

$$\mathbf{Z}_k = \mathbf{Z}_k^{FA} \cup \left(\bigcup_{i=1}^{N_{x,k}} \mathbf{Z}_k^{(i)} \right). \tag{15}$$

Note that the true detection origin (clutter or target?), and the true number of targets, is unknown.

1) Clutter Detection Model: A standard clutter model is used, where the number of clutter detections is modeled as Poisson distributed with rate λ_k and each clutter detection is modeled as independent uniformly distributed in the surveillance area.

2) Target Detection Model: As is common in MTT (see, e.g., [7]), it is assumed that each target generates detections independent of all other targets and that, for each target, the measurements are independent. The detection set likelihood is

$$p\left(\mathbf{Z}_k|\xi_k\right) = N_{z,k}! P\left(N_{z,k}|\xi_k\right) \prod_{j=1}^{N_{z,k}} p\left(\mathbf{z}_k^{(j)} \middle| \xi_k\right). \tag{16}$$

Following [15] and [16], the number of target generated measurements is modeled as Poisson distributed with rate γ_k:

$$P\left(N_{z,k}|\xi_k\right) = P\left(N_{z,k}|\gamma_k\right) = \mathcal{PS}(N_{z,k};\, \gamma_k). \tag{17}$$

The target detections are modeled as being uniform samples across the target surface corrupted by a zero mean Gaussian noise, modeled by the likelihood

$$p\left(\mathbf{z}_k^{(j)} \middle| \xi_k\right) = p\left(\mathbf{z}_k^{(j)} \middle| \mathbf{x}_k, X_k\right) \tag{18a}$$

$$= \mathcal{N}\left(\mathbf{z}_k^{(j)}; H_k\mathbf{x}_k, \rho X_k + R(\mathbf{p}_k)\right) \tag{18b}$$

where $H_k = [\mathbf{I}_2 \quad \mathbf{0}_{2\times 3}]$ and ρ is a scaling parameter. The covariance matrix $R(\mathbf{p})$ models the nonconstant across-range noise variance. It is given by a first-order approximation of the polar to Cartesian conversion of the polar measurement noises σ_r and σ_φ (see, e.g., [7, Section 1.7.2])

$$R(\mathbf{p}) = \mathbf{J}(\mathbf{p})\mathrm{diag}\left(\left[\sigma_r^2,\, \sigma_\varphi^2\right]\right)\mathbf{J}(\mathbf{p})^{\mathrm{T}} \tag{19a}$$

$$\mathbf{J}(\mathbf{p}) = \begin{bmatrix} \cos(\varphi) & -r\sin(\varphi) \\ \sin(\varphi) & r\cos(\varphi) \end{bmatrix} \tag{19b}$$

where r and φ are the range and azimuth corresponding to the position $\mathbf{p}$.

The effective probability of detection is [20]

$$P^e_{k,D}\left(\xi_k^{(i)}\right) = \left(1 - e^{-\gamma_k^{(i)}}\right) P_D \tag{20}$$

where the set of target detections is nonempty with probability $1 - e^{-\gamma_k^{(i)}}$, and the set is detected with probability $P_D \in [0,\, 1]$.

IV. GGIW-PHD Filter for Multiple ETT

The PHD $D_{k|k}(\cdot)$ is, despite its name, not a probability density function. Instead, it is an intensity function whose integral is the expected value of the number of targets (i.e., the estimate of $N_{x,k}$) and whose peaks correspond to likely target locations (i.e., the peaks correspond to the estimates of the target states $\xi_k^{(j)}$); see [9] and [33].

The PHD intensity is typically approximated either using sequential Monte Carlo methods (see [39]) or using distribution mixtures (see [14], [23], and [40]). In this paper, the PHD intensity $D_{k|k}(\cdot)$ at time t_k, given that the measurement sets up to and including time t_k, is approximated by a mixture of GGIW distributions

$$D_{k|k}(\xi_k) = \sum_{j=1}^{J_{k|k}} w_{k|k}^{(j)} \mathcal{GGIW}\left(\xi_k; \zeta_{k|k}^{(j)}\right) \tag{21}$$

where $J_{k|k}$ is the number of components, $w_{k|k}^{(j)}$ is the weight of the jth component, and $\zeta_{k|k}^{(j)}$ is the density parameter of the jth component. In this section, we present a GGIW implementation of the extended target PHD filter presented in [20]. The GGIW-PHD filter is an extension of the GIW-PHD filter presented in [23] and [41], where the measurement rate estimation has been added as outlined in [35]. A flowchart describing the essential parts of the tracking system is shown in Fig. 2. Most of the mathematical details are given in the Appendix. Derivation details are omitted due to page limits.

A. Time Update

Let the prior PHD intensity be of the form (21). The predicted PHD intensity is a GGIW mixture

$$D_{k+1|k}(\xi_{k+1}) = D^b_{k+1}(\xi_{k+1}) + D^s_{k+1|k}(\xi_{k+1}) \tag{22}$$

with two parts corresponding to new targets which appear in the surveillance area (first term) and to targets which persist (i.e., survive) in the surveillance area (second term). Notice that (22) does not take into account spawned targets, i.e., targets that appear close to already existing targets. However, target spawning is typically used to model events such as a target launching another target, e.g., a fighter aircraft launching a missile. Accordingly, in this paper, models for target spawning are not necessary and are thus omitted. Further discussions about spawning within the random matrix extended target model can be found in [42].

The probability that a target persists in the surveillance area is modeled by the probability of survival P_S. For persisting targets, the time evolution is modeled by the dynamic motion models introduced in Section III-B. Additional details are given in the Appendix.

New targets that appear in the surveillance area are modeled by a birth intensity. In previous works on ETT based on the PHD filters, the birth intensities have been modeled as distribution mixtures, where each mixture component corresponds to a location where it is likely to find a new (appearing) target; see [14], [23], and [40]. However, for the data set considered in this paper, there is not an *a priori* knowledge on the regions where the targets are likely to appear. Accordingly, here we use a uniform distribution over the surveillance area for the birth position. The birth measurement rate and extension are modeled as gamma and inverse Wishart distributed, while the velocity and acceleration are modeled as Gaussian distributed.

We use the following intensity for the birth PHD:

$$D_k^b(\xi_k) = w_k^{(b)} \mathcal{U}(\mathbf{p}_k) \mathcal{N}\left([\mathbf{v}_k,\ \omega_k]^{\mathrm{T}}; m_k^{(b)}, P_k^{(b)}\right) \times \mathcal{G}\left(\gamma_k; \alpha_k^{(b)}, \beta_k^{(b)}\right) \mathcal{IW}_d\left(X_k; v_k^{(b)}, V_k^{(b)}\right) \quad (23)$$

where $w_k^{(b)}$ is the birth weight, $m_k^{(b)}$ and $P_k^{(b)}$ are the mean and covariance of the initial velocity and turn rate, $\alpha_k^{(b)}$ and $\beta_k^{(b)}$ define the initial measurement rate, and $v_k^{(b)}$ and $V_k^{(b)}$ define the initial size and shape of the extension. The birth weight models the expected value of the number of new targets that will appear. Additional details are given in the Appendix.

B. Measurement Update

Let the predicted PHD intensity at time t_k be

$$D_{k|k-1}(\xi_k) = D_k^b(\xi_k) + \sum_{j=1}^{J_{k|k-1}} w_{k|k-1}^{(j)} \mathcal{GGIW}\left(\xi_k; \zeta_{k|k-1}^{(j)}\right). \quad (24)$$

The measurement updated PHD intensity is [20]

$$D_{k|k}\left(\xi_k|\mathbf{Z}^k\right) = L_{\mathbf{Z}_k}(\xi_k) D_{k|k-1}\left(\xi_k|\mathbf{Z}^{k-1}\right). \quad (25)$$

where $L_{\mathbf{Z}_k}(\xi_k)$ is the measurement pseudolikelihood. The likelihood $L_{\mathbf{Z}_k}(\xi_k)$ is derived after the measurement model described in Section III-C, and it specifies how the measurement set $\mathbf{Z}_k$ is used to update the PHD intensity. Additional details are given in the Appendix.

For Bayes optimality, the measurement update should consider all possible partitions $\mathcal{P}$ of the measurement set $\mathbf{Z}_k$, but this is not computationally tractable in practice [14], [23], [43]. In this paper, we use the methods from [14] and [23] to compute a subset of partitions. The posterior PHD (25) is a GGIW mixture

$$D_{k|k}(\xi_k) = D_{k|k}^m(\xi_k) + D_{k|k}^b(\xi_k) + D_{k|k}^d(\xi_k) \quad (26)$$

with three parts corresponding to not detected previously existing targets, new targets, and detected previously existing targets.

1) Not Detected Previously Existing Targets: As suggested in [17], we assume that, when a new target is detected, it always generates at least one measurement in the first time step that it appears. This corresponds to the effective probability of detection being unity, $P_{k,D}^e = 1$. Therefore, we only consider missed detections for previously existing targets. See the Appendix for additional details.

2) New Targets: For the PHD corresponding to new targets, the updated positions are Gaussian distributed with means equal to the centroid measurements. This update is approximate, but as shown in [17], the approximation can be justified as long as most of the probability mass of the likelihood is contained inside the surveillance area. See the Appendix for additional details.

3) Detected Previously Existing Targets: The PHD corresponding to detected previously existing targets is updated according to the measurement model (18). See the Appendix for additional details.

C. Postprocessing

1) Mixture Reduction: Due to the association uncertainty (i.e., unknown measurement origin), all MTT methods are affected by an increasing computational complexity; see, e.g., [7] and [9]. In the presented GGIW-PHD filter, the association uncertainty makes the number of components $J_{k|k}$ increase exponentially over time. Therefore, the distribution mixture approximation of the PHD intensity must be reduced at each filter iteration.

In the first step, all components for which either $w_{k|k}^{(j)} < T$ or $\mathrm{E}[\gamma_k] = \alpha_{k|k}^{(j)}/\beta_{k|k}^{(j)} < 1$, or both, are pruned (i.e., discarded). Indeed, components with a low weight can safely be discarded since they represent highly unlikely target states. Moreover, an estimated measurement rate less than one means that, on average, we expect that the target does not generate any detections. Such components can be discarded since targets that do not generate detections cannot be tracked.

In the second step, the component merging is performed. Merging means to find mixture components that are similar enough so that they can be said to represent the same target estimate. Here, merging is performed using modified versions of the methods proposed in [35] and [44].

2) Target Extraction: As mentioned earlier, the peaks in the PHD intensity correspond to likely target states. When the intensity is approximated by a distribution mixture, the peaks are given by the mixture components with large weights $w_{k|k}^{(j)}$ [14], [23], [40]. In particular, for each time step, the set of extracted targets is computed by taking the GGIW components for which $w_{k|k}^{(j)} > \bar{w}_0$, where $\bar{w}_0$ is the extraction threshold. Accordingly, the target extraction step provides

$$\hat{\mathbf{X}}_{k|k} = \left\{\hat{\xi}_{k|k}^{(i)}\right\}_{i:1}^{\hat{N}_{k|k}},\ \ \hat{\xi}_{k|k}^{(i)} = \left(\mathrm{E}\left[\gamma_k\right], \mathrm{E}\left[\mathbf{x}_k\right], \mathrm{E}\left[X_k\right]\right) \quad (27)$$

where the expected values are with respect to the GGIW component. The set $\hat{\mathbf{X}}_{k|k}$ is an estimate of the set $\mathbf{X}_k$ defined in (1).

3) Track Estimation: To enable the target track estimation, we exploit a label scheme [45], [46]. In particular, we assign to each GGIW component a label $\ell_{k|k}^{(j)}$, whose initial value is 0. If the component is extracted and a label has not yet been assigned (i.e., $\ell_{k|k}^{(j)} = 0$), a unique positive integer is assigned to the label. The assigned labels are kept in the time update and measurement update steps.

A track estimate $\hat{\mathcal{T}}_{k|k}^{(j)}$ is considered confirmed if a GGIW component with an assigned label is extracted for at least three consecutive time steps. The track estimates remain confirmed until the corresponding GGIW components are pruned from the PHD intensity. This procedure effectively minimizes the number of false target tracks, but it comes at the price of a delay in the confirmation of the track estimates.

Label management is performed in the mixture reduction step to ensure that, after each iteration, all the labels are unique. During the component merging, the following actions are performed.

1) If $\ell_{k|k}^{(j)} = 0$, the component is not merged with any other component.
2) Two components j and i are candidates for merging only if $\ell_{k|k}^{(j)} = \ell_{k|k}^{(i)}$ and the symmetric Kullback–Leibler divergence (KL-div) between the two components is less than a threshold U; see [35] and [44].
3) Components are merged so that the merged weight $\tilde{w}_{k|k}^{(j)}$ is smaller than a threshold $\bar{w}_1$.

After, the merging label management is performed as follows. Let L be a set of GGIW components with identical assigned labels. If

$$\max_{j \in L} \; w_{k|k}^{(j)} \geq \bar{w}_2 \vee \frac{\max_{j \in L} w_{k|k}^{(j)}}{\sum_{j \in L} w_{k|k}^{(j)}} > \bar{w}_3 \tag{28}$$

(with $\vee$ being the logical "or"), then all components are pruned except the one with the maximum weight. Otherwise, let the maximum weight component keep the assigned label, and reset $\ell_{k|k}^{(j)} = 0$ for the remaining components.

V. Experimental Results

In this section, we describe the acquisition system used to collect the real data through which we assess the ETT performance of the proposed GGIW-PHD filter. We also provide details about the strategy employed to get the detection measurements from the considered radar data. Finally, we present and discuss the obtained ETT results.

The parameters relevant to the acquisition system, the detector, and the GGIW-PHD filter are given in Table III.

TABLE III
System Parameters

Acquisition system		**Value**
Antenna rotation period	Δt	2.41 s
Range resolution	Δr	7.2 m
Azimuth resolution	$\Delta\varphi$	0.35°
Radar scale		3679 m
View angular sector		260°
Radar's height (over sea level)		15 m

OS-CFAR detector		**Value**
False alarm probability	PFA	10^{-9}
Reference window samples	M	$32(16 \times 2)$
Guard cells	G	$8(4 \times 2)$
Noise level representative rank	k	$24(0.75\text{M})$

GGIW-PHD filter		**Value**
Sampling time	T_s	Δt
Forgetting factor	η_k	1.05
Kinematics noise	σ_a, σ_ω	0.1, $\frac{0.1\pi}{180T_s}$
Extension uncertainty	n	100
Temporal decay	τ	120
Scaling parameter	ρ	1/4
Measurement noise	σ_r, σ_φ	$\Delta r/2$, $\Delta\varphi/2$
Clutter density	$\beta_{FA,k}$	$100/V(\mathcal{A})$
Detection probability	P_D	0.99
Survival probability	P_S	0.99
Birth weight	$w_k^{(b)}$	10^{-2}
Birth mean	$m_k^{(b)}$	$\mathbf{0}_{3\times 1}$
Birth covariance	$P_k^{(b)}$	$\text{diag}\left(1,\ 1,\ \frac{0.01\pi}{180T_s}\right)$
Birth rate	$\alpha_k^{(b)}$, $\beta_k^{(b)}$	0.04, 0.008
Birth extension	$v_k^{(b)}$, $V_k^{(b)}$	120, $0.01\mathbf{I}_d$
Extraction threshold	$\bar{w}_0$	0.5
Pruning threshold	T	10^{-3}
Merging threshold	U	25
Weight thresholds	$\bar{w}_1$, $\bar{w}_2$, $\bar{w}_3$	1.1, 1, 0.8

A. Acquisition System and Setup

Data were collected on October 1, 2013 by an incoherent X-band marine radar mounted at Giglio Island, in Tuscany (Italy). Recall that these systems are raising an increasing interest for the wave motion monitoring since a number of inversion approaches have been developed and validated in the last two decades to estimate the sea state parameters, the sea surface currents, and bathymetry fields starting from the analysis of marine X-band radar signals; see, e.g., [47]–[50]. According to these appealing capabilities, the data considered in this paper were acquired by the X-band marine radar employed to both monitor the sea conditions and support the removal activities of the Costa Concordia wreckage, the cruise ship that capsized and partially sank close to the harbor of Giglio Island in January 2012 [21].

Here, we consider a data set composed of 217 consecutive radar images relevant to an acquisition interval of about 10 min, from 8:15 A.M. to 8:25 A.M. (UTC). A wind intensity of about 1 m/s and a wave height less than 0.5 m (corresponding to "smooth sea" conditions in the Douglas scale) were measured at Giglio Island during the radar acquisition period [51]–[55].

It is worth noting that the removal operations of the Costa Concordia caused an increase in the number of targets compared to traffic conditions usually observed at the harbor of Giglio Island. Accordingly, multiple objects were present within the radar's surveillance space during the acquisition period, including moving boats and steady targets like buoys, rocks, platforms, and fixed boats. Among the moving boats, two vessels, here labeled T1 and T2, are of increased interest because they moved through the surveillance area for extended periods of time.

Target T1 was a boat involved in the management of the Costa Concordia wreckage. It was followed by the radar for about 80 scans (just over 3 min) before it moved behind the wreckage, thus disappearing from the radar's view. Its dimensions are unknown.

Target T2 was a ferry boat that approached Giglio Island. It was followed by the radar for about 170 scans (almost 7 min). During this observation period, T2 started in the far

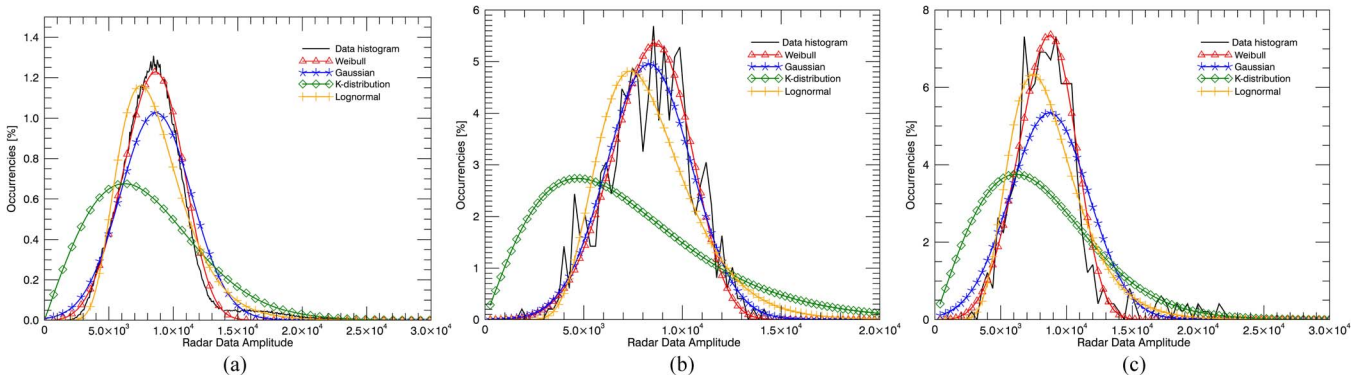

Fig. 3. Distribution fitting. (a) Data histogram of a sample radar scan compared with some theoretical distributions. (b) Comparison relevant to a single azimuth direction containing only the clutter component. (c) Comparison relevant to a single azimuth direction that contains radar echoes arising from both targets and the sea surface.

range and moved closer to the harbor with a heading approximately pointing directly at the sensor. Its dimensions are approximately 70 m $\times$ 15 m (length $\times$ width).

B. Detection Strategy

In our processing chain, each polar radar image is subjected to a pulse integration step before undergoing the detection procedure. Pulse integration is aimed at enhancing the target detection probability and is based on the sum of $N_{ra}^I \times N_{az}^I$ (range $\times$ azimuth) contiguous samples of the polar radar scans. The data considered in this paper were processed using $N_{ra}^I = 2$ and $N_{az}^I = 4$.

After the pulse integration step, each radar scan is processed through an OS-CFAR detector [56], [57]. Recall that CFAR algorithms are founded on the knowledge of the statistical distribution describing the sea clutter since they resort to this information to compute the local detection threshold [58]. Therefore, a statistical analysis was carried out on the radar data to find the best model for the sea-clutter description. To this aim, for each radar scan, we compared the empirical distribution of the actual data with a number of theoretical probability distributions, namely, the Gaussian, the log-normal, the Weibull, and the K-distribution. These probability distributions are widely employed to model the sea clutter observed in high-resolution radar data; see, e.g., [1]–[3], [5], and [6]. The distribution fitting requires the estimation of the characteristic parameters (i.e., the mean and the standard deviation or the scale and shape parameters) of each theoretical model from the radar data [3], [59], [60]. Accordingly, we repeated the parameter estimation procedure for each radar scan to evaluate the best model in describing the clutter in the considered data set. The goodness of fit provided by each model was tested with the Kolmogorov–Smirnov procedure [61], whose results over the whole data set led us to assume the Weibull distribution for the clutter description.

The comparison between the histogram of a sample radar image and the fitted theoretical densities is shown in Fig. 3(a). It clearly shows that the estimated Weibull distribution fits better to data compared to the other models. In particular, the Weibull distribution matches very well with the main mode of the data histogram, which is peaked around an amplitude value of about 0.85×10^4 and is representative of radar echoes arising from the sea surface. The fits provided by the other models are not as good because they suffer more from the radar echoes arising from targets. Target echoes exhibit higher amplitudes and are responsible of the secondary mode observed in the data histogram, which is peaked around an amplitude value of about 1.55×10^4. Therefore, for the considered data set, the Weibull distribution represents a very good model to get only the clutter characteristics from the overall (target and clutter) radar signal. Similar results also apply when the distribution fitting is carried out separately on each range line (i.e., a line from the polar radar image corresponding to a fixed azimuth direction), as can be observed from Fig. 3(b) and (c). This is actually the case of most practical interest because, usually, CFAR algorithms provide detection results by processing a single range line at a time. The outputs of the considered OS-CFAR detector are then converted from polar to Cartesian coordinates, as explained in Section III-C. A sample of the detector's output in Cartesian coordinates is shown in Fig. 4(a).

C. Extended Target Tracker Results

For each radar scan, the GGIW-PHD filter is fed with the Cartesian detection measurements. Due to the high resolution of the acquisition system, each actual target is represented by a cluster of detections. False alarms can give rise to either punctual detections or clusters of multiple detections. Fig. 4(b) shows the output from the GGIW-PHD filter corresponding to the detections of Fig. 4(a). The detection clusters (i.e., the actual targets) are properly mapped into ellipses during the tracking procedure, as the comparison between Fig. 4(a) and (b) clearly shows. Recall that the shape of each ellipse is due to the use of the random matrix extended target model [18]. In Fig. 5, the number of confirmed track estimates is compared to the number of extracted targets. As can be observed, the number of confirmed track estimates has a slower initial response time, but it also exhibits less variability compared to the number of targets (cardinality) estimated at each time step. The lower variability and the fact that the number of confirmed track estimates is smaller than the number of extracted targets show that the sensitivity to false alarms and missed detections is lowered when the proposed target track label scheme is used. The positions corresponding to all confirmed track estimates are shown in Fig. 6, where the estimated tracks for T1 and T2 are labeled.

In Fig. 7, we show the detailed estimated tracks for T1 and T2, and in Fig. 8, we show their estimated velocities, headings, and turn rates, while their estimated lengths, widths, and measurement rates are shown in Fig. 9. Global Positioning System (GPS) data are unfortunately not available for neither T1 nor T2, so instead of comparing the ETT results to the ground truth, we discuss the rationality of the outputs provided by the GGIW-PHD filter.

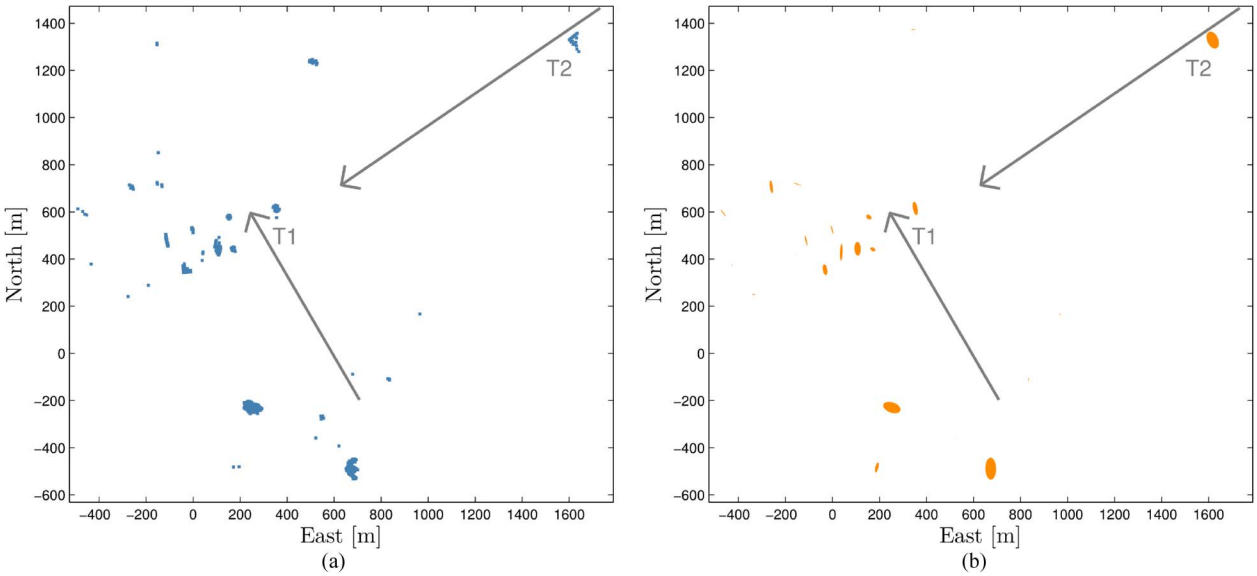

Fig. 4. (a) Sample of the detector's output in Cartesian coordinates (the sensor is in the origin). The gray arrows represent approximations of the trajectories of T1 and T2. (b) Output of the GGIW-PHD filter (orange ellipses) relevant to the detections (blue clusters) of Fig. 4(a). Ellipses for T1 and T2 are located just above the markers.

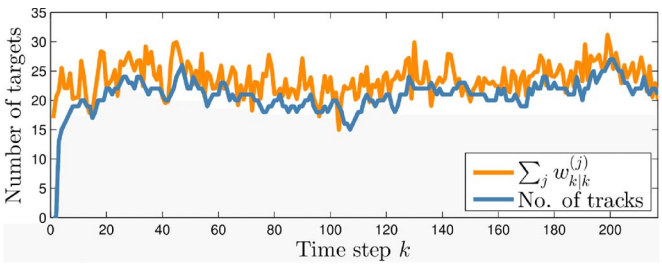

Fig. 5. Comparison between (orange solid line) the estimated cardinality and (blue solid line) the number of confirmed track estimates.

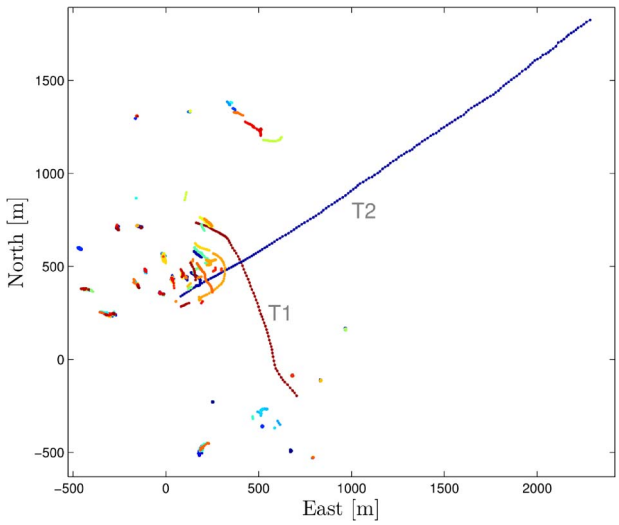

Fig. 6. All the confirmed target track estimates, each shown with a unique color. The long tracks corresponding to T1 and T2 clearly stand out.

In particular, the kinematic state estimates, observed in Figs. 7 and 8, appear to be good. The estimated positions (the centers of the ellipses in Fig. 7) together form smooth track estimates. The quick reduction in the velocity of T1 around time step 50 is caused by the boat's maneuvering to go behind the Costa Concordia. The slower reduction in the velocity of T2 starting at time step 120 is caused by the ferry's gradual slowing during its entrance at the harbor. This is a reasonable estimate, as speed limits are typically enforced in and around harbors. In terms of the heading and turn-rate estimates, the estimates for T1 properly capture the small turns to the right and left, and the heading of T2 is correctly estimated as approximately constant with zero turn rate.

The estimation results for the shapes of T1 and T2 are instead less satisfactory than what the results for the kinematics are. Although the estimated shapes exhibit a quite smooth behavior against time [i.e., the shape of the estimated ellipses does not vary as much as the underlying detection clusters do (see Fig. 7)], significant variations in both the width and length estimates can be observed during the monitoring period, particularly for target T2 (see Fig. 9).

In particular, vessels' shape estimates suffer from the distortions introduced during the data acquisition process, which, in turn, depend on the vessels' position as well as on some of the characteristics of the radar, including the height, the resolution, and the point spread function.

Results of these distortions, and their effects on the shape retrieval, can be clearly observed from the detection clusters relevant to target T2 [see Fig. 7(b)]. The mean number of detected samples in both the along-range and across-range directions increases when T2 approaches the radar (this is confirmed by the measurement rate estimates of Fig. 9). In addition, the across-range size of each detected sample decreases as the distance between the radar and T2 reduces. As a consequence, at the beginning of the observation period, the detection clusters are wider than long, while their shape becomes progressively long and narrow as T2 approaches the radar.

These behaviors are due to the joint effect of shadowing, point spread function, and space variance of the across-range resolution, which distort target mapping in radar data and consequently, affect the shape of the detection clusters.

Recall that T2 moves in a radial direction toward the radar and its length (along-range dimension) is about 70 m, while its

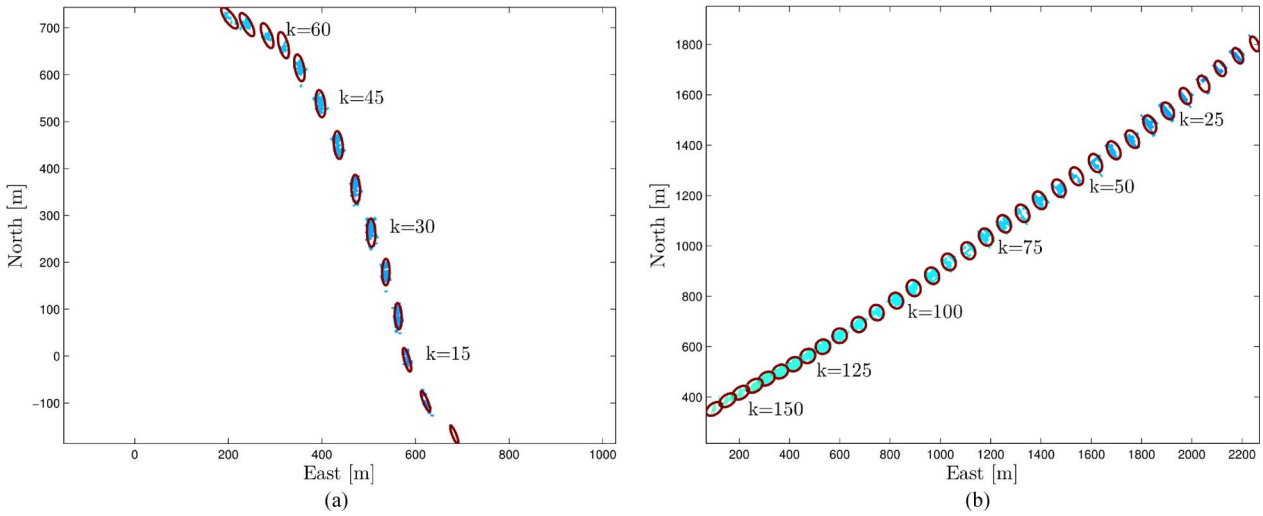

Fig. 7. Tracking history of the extended targets (a) T1 and (b) T2. For every fifth time steps, the detections are shown using a color ranging from blue (first time step) to green (last time step). The flags represent the time steps, while the estimated extensions are shown as red ellipses.

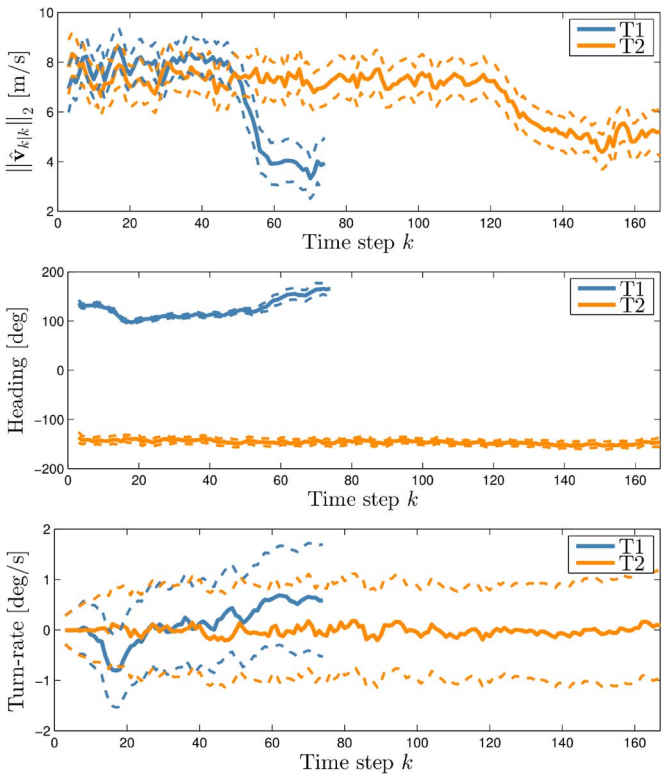

Fig. 8. Estimated velocities, headings, and turn rates for targets T1 and T2. Estimates are shown as solid lines, and uncertainty regions are shown as dashed lines.

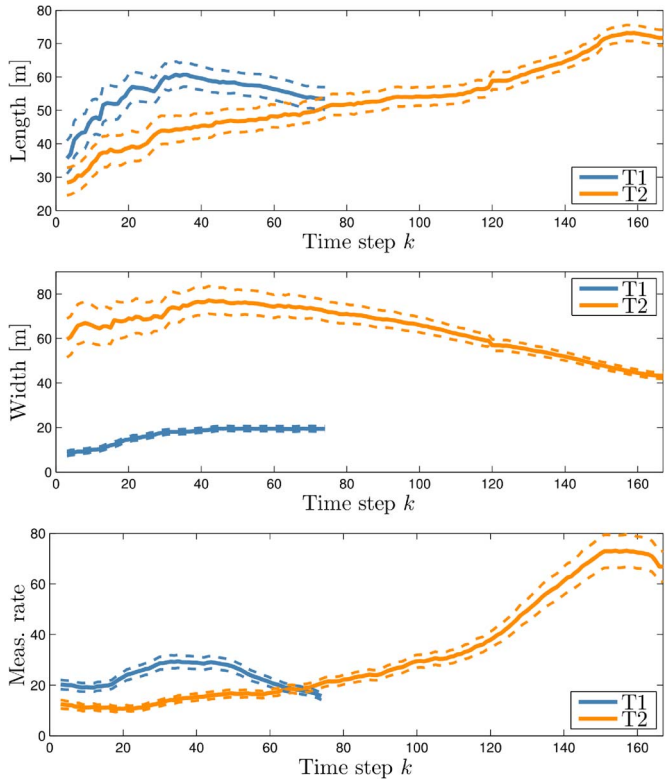

Fig. 9. Estimated lengths, widths, and measurement rates for targets T1 and T2. Estimates are shown as solid lines, and uncertainty regions are shown as dashed lines.

width (across-range dimension) is approximately 15 m. Therefore, since the range resolution is $\Delta r = 7.2$ m (see Table III), the actual vessel length fits into about 10 resolution cells in the along-range direction. Nevertheless, at the beginning of the observation period (e.g., $k \approx 10$), T2 exhibits a comparatively large distance r from the radar ($x \approx 2200$ m, $y \approx 1750$ m; $r \approx 2800$ m), so most of the vessel poop deck is masked by the vessel prow because of the shadowing phenomenon. Accordingly, at such a distance, this distortion gives rise to clusters having a scarce number of detections [from 1 to 6; see the clusters in Fig. 7(b)] in the along-range direction, thus leading to initial length estimates of about 30 m (see Fig. 9).

However, shadowing mainly occurs if the target is observed from the radar with a large look angle, i.e., if the target to radar distance is large. On the other hand, shadowing reduction improves the sight of the along-range dimension of the vessel. An increasing number of radar echoes arising from the revealing parts of the target can indeed be expected as the ferry boat moves toward the harbor. This is confirmed by the mean number of along-range detections [see Fig. 7(b)], which increases

while T2 approaches the radar. As expected, this turns into an improvement of the length estimates, which increase steadily until they settle on a value around 70 m, which is the actual length of target T2.

As concerns the width estimates for target T2, they suffer from both the space variance of the across-range resolution and the effects of the point spread function.

The across-range resolution $\Delta\chi$ of a real aperture radar is indeed a linear function of the range, i.e., $\Delta\chi \approx r\Delta\varphi$, where $\Delta\varphi$ represents the bearing resolution (in radians) of the system. As a consequence, the across-range size of the detection samples increases with the distance from the radar. This means that, at far range, the across-range dimension of a target which moves in a radial direction is, in principle, mapped into only one detection sample, independently of the value W of the target's width. This happens until the target reaches a distance $r_{\min}$, where the across-range resolution $\Delta\chi$ becomes equal to W. Once this distance is approached, radar echoes arising from the across-range dimension of the target are mapped into more resolution cells (and then into more detection samples), whose number depends upon the ratio between W and the local value of $\Delta\chi$. Therefore, the larger the range from radar to target is, the greater the uncertainty on the across-range dimension of the target. This is confirmed by the behavior of the uncertainty region relevant to the width estimates of T2 (see Fig. 9).

Since, at the beginning of the observation period ($k \approx 10$; $r \approx 2800$ m), the across-range resolution is $\Delta\chi \approx 17$ m, then the actual width of target T2 should be mapped into 1 or 2 detection samples in the across-range direction. In spite of this, from Fig. 7(b), it can be observed that, at far range, the detection clusters exhibit about 4–5 samples in the across-range direction. This is caused by the convolution-like effects introduced by the radar point spread function, which smears the target's energy over several resolution cells [62], thus leading to an increased number of detections in the across-range direction. Therefore, due to the value of the across-range resolution and to the smearing effects of the point spread function, the far range "apparent" width of T2 should be about 70–80 m. However, this exaggerated width effect is partly alleviated by modeling the noise covariance $R(\cdot)$ in (18), whose usage allows us to get initial width estimates of about 60 m. During its route, T2 reduces its distance from the radar, and then, it is mapped into more and more resolution cells. For instance, at $k \approx 145$ ($x \approx 350$ m, $y \approx 450$ m; $r \approx 570$ m), we have $\Delta\chi \approx 3.5$ m and the actual width of target T2 should be mapped into 4–6 detection samples in the across-range direction. Nevertheless, due to the point spread function, the across-range dimension of the vessel is smeared into more than ten resolution cells, thus leading to width estimates of about 40 m.

The results obtained and presented here suggest that the estimation results for the shape of T2 suffer from the deceptive radar measurements that we provide to the GGIW-PHD filter. As stated, the latter come from the space-variant distortions which affect the mapping of T2 in radar data while the target covers its route. These extremely unfavorable conditions (i.e., the heavy shadowing and the deep variations in mapping the across-range dimension of the vessel) can probably be considered as the worst case to deal with ETT problems from radar data.

TABLE IV
COMPUTATIONAL TIMES OF THE GGIW-PHD FILTER (MILLISECONDS)

Operation	Mean	St.dev.	Min	Max
Measurement set partitioning	106	25	42	205
Prediction and correction	1115	399	209	2604
Mixture reduction	351	103	184	731
Extraction and maintenance	0.9	0.6	0.4	10
Total	1573	467	546	3193

The same considerations would also apply to target T1. However, compared to T2, the size estimates for T1 exhibit smaller variations and seem to be reasonable. This happens because, during the observation period, the distance between T1 and the radar does not change as much as the distance between the radar and T2. Therefore, the shape of the detection clusters of T1 does not suffer from the same heavy distortions which affect target T2.

To summarize, the results show that the proposed ETT system can accurately estimate the target kinematics at all sensor-to-target ranges. However, due to the shadowing, the sensor resolution, and the point spread function, the shape and size estimation is inaccurate at larger sensor-to-target ranges.

Of course, targets' shape retrieval from radar data needs further investigations. However, it is worth to note that, probably, the shape estimation results of an ETT system could be greatly improved. In this regard, it could be useful to acquire radar data from more favorable (higher) positions, as to reduce the shadowing effect and provide more accurate estimates of the targets' along-range dimension even at the far ranges. In addition, some *ad hoc* deconvolution techniques aimed at reducing the smearing effects due to the point spread function could also be applied on radar data as to improve the size estimates in the across-range dimension.

D. Computational Times

The average time required to get the detection output from a single radar scan is about 0.6 s. The computational times required to perform a single tracking cycle through the GGIW-PHD filter are reported in Table IV. The average time for a single filter cycle is less than 1.6 s, meaning that, on average, one iteration of the target tracking system takes 2.2 s. These computational times allow us to complete the one processing cycle within one antenna's rotation period (2.41 s). The filter was implemented in MATLAB to run on a 2.83-GHz Intel Core2 Quad CPU with 3.48 GB of RAM and was not optimized for speed. By optimizing the code and by porting the system to low-level programming languages, a considerable speedup can be expected.

VI. CONCLUSION AND FUTURE WORK

Real-world radar images, acquired on October 2013 by a coastal incoherent X-band radar, during the recovery operations of the Costa Concordia wreckage in Tuscany, Italy, have been processed by the proposed ETT system. The real-time requirement of the surveillance application has been satisfied by using a first stage of detection (OS-CFAR) and a second stage of tracking (GGIW-PHD). Experimental results have been reported and discussed, showing the capability of the proposed

ETT methodology to deal with clutter and with multiple close-spaced targets that appear and disappear in time.

Some considerations of the nonideal effects present in the experimental data, common to every real aperture radar, have been provided in relation to the assumptions made for the tracking procedure and the geometry of the system. In particular, a degradation in the estimates of the targets' shape has been observed in relation to the range of the targets. Such a degradation arises from the distortions introduced by the imaging process that has not been yet taken into account in currently available ETT tracking models. An important topic for future works should be the improvement of these models, e.g., the application of postprocessing techniques which allow better capturing of the aforementioned distortions, thus improving the targets' shape retrieval from radar data.

APPENDIX A
GGIW-PHD FILTER DETAILS

A. Time Update for Surviving Existing Targets

The PHD intensity corresponding to existing targets that remain in the surveillance area is

$$D^s_{k+1|k}(\xi_{k+1}) = \sum_{j=1}^{J_{k|k}} w^{(j)}_{k+1|k}\mathcal{GGIW}\left(\xi_{k+1};\zeta^{(j)}_{k+1|k}\right) \tag{29a}$$

$$w^{(j)}_{k+1|k} = P_S w^{(j)}_{k|k} \tag{29b}$$

$$\alpha^{(j)}_{k+1|k} = \frac{\alpha^{(j)}_{k|k}}{\eta_k}, \quad \beta^{(j)}_{k+1|k} = \frac{\beta^{(j)}_{k|k}}{\eta_k} \tag{29c}$$

$$m^{(j)}_{k+1|k} = \mathbf{f}\left(m^{(j)}_{k|k}\right) \tag{29d}$$

$$P^{(j)}_{k+1|k} = \mathbf{F}^{(j)}_{k|k}P^{(j)}_{k|k}\left(\mathbf{F}^{(j)}_{k|k}\right)^{\mathrm{T}} + \mathbf{Q} \tag{29e}$$

$$v^{(j)}_{k+1|k} = 2d + 2 + e^{-T_s/\tau}\left(v^{(j)}_{k|k} - 2d - 2\right) \tag{29f}$$

$$V^{(j)}_{k+1|k} = \left(v^{(j)}_{k+1|k} - 2d - 2\right)\left(v^{(j)}_{k|k} - 2d - 2\right)^{-1} \times M\left(m^{(j)}_{k|k}\right)V^{(j)}_{k|k}M\left(m^{(j)}_{k|k}\right)^{\mathrm{T}} \tag{29g}$$

where $\mathbf{F}^{(j)}_{k|k}$ is the Jacobian of $\mathbf{f}(\mathbf{x})$ with respect to $\mathbf{x}$ evaluated at $m^{(j)}_{k|k}$.

B. Measurement Update

1) Measurement Pseudolikelihood: The measurement pseudolikelihood is [20]

$$L_{\mathbf{Z}_k}(\xi_k) \triangleq 1 - P^e_{k,D} + e^{-\gamma_k}P_D\sum_{\mathcal{P}\angle\mathbf{Z}_k}\omega_{\mathcal{P}}\sum_{\mathbf{W}\in\mathcal{P}}\frac{\gamma_k^{|\mathbf{W}|}}{d_{\mathbf{W}}}\prod_{\mathbf{z}_k\in\mathbf{W}}\frac{\phi_{\mathbf{z}_k}(\xi_k)}{\lambda_k c_k(\mathbf{z}_k)} \tag{30}$$

where

- the first part corresponds to missed detections, and the second part corresponds to detected targets;
- the quantities $\omega_{\mathcal{P}}$ and $d_{\mathbf{W}}$ are nonnegative coefficients defined, for each partition $\mathcal{P}$ and cell $\mathbf{W}$, respectively, as

$$\omega_{\mathcal{P}} = \frac{\prod_{\mathbf{W}\in\mathcal{P}} d_{\mathbf{W}}}{\sum_{\mathcal{P}'\angle\mathbf{Z}_k}\prod_{\mathbf{W}'\in\mathcal{P}'} d_{\mathbf{W}'}} \tag{31a}$$

$$d_{\mathbf{W}} = \delta_{|\mathbf{W}|,1} + D_{k|k-1}\left[P_D\gamma_k^{|\mathbf{W}|}e^{-\gamma_k}\prod_{\mathbf{z}_k\in\mathbf{W}}\frac{\phi_{\mathbf{z}_k}(\cdot)}{\lambda_k c_k(\mathbf{z}_k)}\right]. \tag{31b}$$

- $\phi_{\mathbf{z}_k}(\xi_k) \triangleq p(\mathbf{z}_k|\xi_k)$ is the likelihood function for a single target generated measurement, given in (18).

2) Not Detected Previously Existing Targets: The updated PHD corresponding to previously existing targets that are not detected is

$$D^m_{k|k}(\xi_k) = \sum_{j=1}^{J_{k|k-1}}\left(1 - P^e_{k,D}\right)w^{(j)}_{k|k-1}\mathcal{GGIW}\left(\xi_k;\zeta^{(j)}_{k|k-1}\right) \tag{32a}$$

$$= \sum_{j=1}^{J_{k|k-1}} p^{(j)}(\gamma_k)\mathcal{N}\left(\mathbf{x}_k;m^{(j)}_{k|k},P^{(j)}_{k|k}\otimes X_k\right) \times \mathcal{IW}_d\left(X_k;v^{(j)}_{k|k},V^{(j)}_{k|k}\right) \tag{32b}$$

where $p^{(j)}(\gamma_k)$ is

$$p^{(j)}(\gamma_k) = (1-P_D)w^{(j)}_{k|k-1}\mathcal{G}\left(\gamma_k;\alpha^{(j)}_{k|k},\beta^{(j)}_{k|k}\right) + P_D\left(\frac{\beta^{(j)}_{k|k}}{\beta^{(j)}_{k|k}+1}\right)^{\alpha^{(j)}_{k|k}} w^{(j)}_{k|k-1}\mathcal{G}\left(\gamma_k;\alpha^{(j)}_{k|k},\beta^{(j)}_{k|k}+1\right). \tag{33}$$

Using gamma-mixture reduction (see [35]), $p^{(j)}(\gamma_k)$ is approximated as

$$\tilde{p}^{(j)}(\gamma_k) = \tilde{w}^{(j)}_{k|k}\mathcal{G}\left(\gamma_k;\tilde{\alpha}^{(j)}_{k|k},\tilde{\beta}^{(j)}_{k|k}\right). \tag{34}$$

This gives the PHD intensity approximation

$$D^m_{k|k}(\xi_k) \approx \sum_{j=1}^{J_{k|k-1}}\tilde{w}^{(j)}_{k|k}\mathcal{GGIW}\left(\xi_k;\tilde{\zeta}^{(j)}_{k|k}\right) \tag{35}$$

where $\tilde{\zeta}^{(j)}_{k|k} = \{\tilde{\alpha}^{(j)}_{k|k},\tilde{\beta}^{(j)}_{k|k},m^{(j)}_{k|k-1},P^{(j)}_{k|k-1},v^{(j)}_{k|k-1},V^{(j)}_{k|k-1}\}$.

3) New Targets: The PHD corresponding to new targets is

$$D^b_{k|k}(\xi_k) = \sum_{\mathcal{P}\angle\mathbf{Z}_k}\sum_{\mathbf{W}\in\mathcal{P}} w^{(b,\mathbf{W})}_{k|k}\mathcal{GGIW}\left(\xi_k;\zeta^{(b,\mathbf{W})}_{k|k}\right) \tag{36a}$$

$$\alpha^{(b,\mathbf{W})}_{k|k} = \alpha^{(b)}_k + |\mathbf{W}|, \quad \beta^{(b,\mathbf{W})}_{k|k} = \beta^{(b)}_k + 1 \tag{36b}$$

$$m^{(b,\mathbf{W})}_{k|k} = \left[\left(\bar{z}^{\mathbf{W}}_k\right)^{\mathrm{T}}, \left(m^{(b)}_k\right)^{\mathrm{T}}\right]^{\mathrm{T}} \tag{36c}$$

$$P^{(b,\mathbf{W})}_{k|k} = \mathrm{blkdiag}\left(Z^{\mathbf{W}}_k/|\mathbf{W}|, P^{(b)}_k\right) \tag{36d}$$

$$v^{(b),\mathbf{W}}_{k|k} = v^{(b)}_{k|k-1} + |\mathbf{W}| - 1 \tag{36e}$$

$$V^{(b),\mathbf{W}}_{k|k} = V^{(b)}_{k|k-1} + Z^{\mathbf{W}}_k. \tag{36f}$$

4) Detected Previously Existing Targets: The updated PHD corresponding to detected previously existing targets is

$$D^{d}_{k|k}(\xi_k) = \sum_{\mathcal{P}\angle\mathbf{Z}_k}\sum_{\mathbf{W}\in\mathcal{P}}\sum_{j=1}^{J_{k|k-1}} w^{(j,\mathbf{W})}_{k|k}\mathcal{GGIW}\left(\xi_k;\zeta^{(j,\mathbf{W})}_{k|k}\right) \tag{37a}$$

$$\alpha^{(j,\mathbf{W})}_{k|k} = \alpha^{(j)}_{k|k-1} + |\mathbf{W}|, \quad \beta^{(j,\mathbf{W})}_{k|k} = \beta^{(j)}_{k|k-1} + 1 \tag{37b}$$

$$m^{(j,\mathbf{W})}_{k|k} = m^{(j)}_{k|k-1} + K^{(j,\mathbf{W})}_{k|k-1}\varepsilon^{(j,\mathbf{W})}_{k|k-1} \tag{37c}$$

$$P^{(j,\mathbf{W})}_{k|k} = P^{(j)}_{k|k-1} - K^{(j,\mathbf{W})}_{k|k-1}H_k P^{(j)}_{k|k-1} \tag{37d}$$

$$v^{(j,\mathbf{W})}_{k|k} = v^{(j)}_{k|k-1} + |\mathbf{W}| \tag{37e}$$

$$V^{(j,\mathbf{W})}_{k|k} = V^{(j)}_{k|k-1} + \hat{N}^{(j,\mathbf{W})}_{k|k-1} + \hat{Z}^{(j,\mathbf{W})}_{k|k-1} \tag{37f}$$

$$\hat{X}^{(j)}_{k|k-1} = V^{(j)}_{k|k-1}\left(v^{(j)}_{k|k-1} - 2d - 2\right)^{-1} \tag{37g}$$

$$\hat{R}^{(j,\mathbf{W})}_{k|k-1} = \rho\hat{X}^{(j)}_{k|k-1} + R\left(H_k m^{(j)}_{k|k-1}\right) \tag{37h}$$

$$\varepsilon^{(j,\mathbf{W})}_{k|k-1} = \bar{\mathbf{z}}^{\mathbf{W}}_k - H_k m^{(j)}_{k|k-1} \tag{37i}$$

$$N^{(j,\mathbf{W})}_{k|k-1} = \varepsilon^{(j,\mathbf{W})}_{k|k-1}\left(\varepsilon^{(j,\mathbf{W})}_{k|k-1}\right)^{\mathrm{T}} \tag{37j}$$

$$S^{(j,\mathbf{W})}_{k|k-1} = H_k P^{(j)}_{k|k-1}H_k^{\mathrm{T}} + \frac{\hat{R}^{(j,\mathbf{W})}_{k|k-1}}{|\mathbf{W}|} \tag{37k}$$

$$K^{(j,\mathbf{W})}_{k|k-1} = P^{(j)}_{k|k-1}H_k^{\mathrm{T}}\left(S^{(j,\mathbf{W})}_{k|k-1}\right)^{-1} \tag{37l}$$

$$\hat{Z}^{(j,\mathbf{W})}_{k|k-1} = \left(\hat{X}^{(j)}_{k|k-1}\right)^{1/2}\left(\hat{R}^{(j,\mathbf{W})}_{k|k-1}\right)^{-1/2} Z^{\mathbf{W}}_k \times \left(\hat{R}^{(j,\mathbf{W})}_{k|k-1}\right)^{-\mathrm{T}/2}\left(\hat{X}^{(j)}_{k|k-1}\right)^{\mathrm{T}/2} \tag{37m}$$

$$\hat{N}^{(j,\mathbf{W})}_{k|k-1} = \left(\hat{X}^{(j)}_{k|k-1}\right)^{1/2}\left(S^{(j,\mathbf{W})}_{k|k-1}\right)^{-1/2} N^{(j,\mathbf{W})}_{k|k-1} \times \left(S^{(j,\mathbf{W})}_{k|k-1}\right)^{-\mathrm{T}/2}\left(\hat{X}^{(j)}_{k|k-1}\right)^{\mathrm{T}/2} \tag{37n}$$

5) Weights: The weights of the GGIW components corresponding to detected targets are

$$w^{(b,\mathbf{W})}_{k|k} = \frac{\omega_{\mathcal{P}}\mathcal{L}^{(b,\mathbf{W})}_k w^{(b)}_k}{d_{\mathbf{W}}\beta^{|\mathbf{W}|}_{FA,k}V(\mathcal{A})} \tag{38a}$$

$$w^{(j,\mathbf{W})}_{k|k} = \frac{\omega_{\mathcal{P}}P_D\mathcal{L}^{(j,\mathbf{W})}_k w^{(j)}_{k|k-1}}{d_{\mathbf{W}}\beta^{|\mathbf{W}|}_{FA,k}} \tag{38b}$$

$$d_{\mathbf{W}} = \delta_{|\mathbf{W}|,1} + \frac{\mathcal{L}^{(b,\mathbf{W})}_k w^{(b)}_k}{\beta^{|\mathbf{W}|}_{FA,k}V(\mathcal{A})} + \sum_{j=1}^{J_{k|k-1}}\frac{P_D\mathcal{L}^{(j,\mathbf{W})}_k w^{(j)}_{k|k-1}}{\beta^{|\mathbf{W}|}_{FA,k}} \tag{38c}$$

$$\mathcal{L}^{(b,\mathbf{W})}_k = \frac{|\mathbf{W}|^{-d/2}}{\pi^{|\mathbf{W}|(d-1)/2}}\frac{\Gamma_d\left(\frac{v^{(b,\mathbf{W})}_{k|k}}{2}\right)\left|V^{(b)}_k\right|^{\frac{v^{(b)}_k-d-1}{2}}}{\Gamma_d\left(\frac{v^{(b)}_k}{2}\right)\left|V^{(b,\mathbf{W})}_{k|k}\right|^{\frac{v^{(b,\mathbf{W})}_{k|k}-d-1}{2}}} \times \frac{\Gamma\left(\alpha^{(b,|\mathbf{W}|)}_{k|k}\right)\left(\beta^{(b)}_k\right)^{\alpha^{(b)}_k}}{\Gamma\left(\alpha^{(b)}_k\right)\left(\beta^{(b,\mathbf{W})}_{k|k}\right)^{\alpha^{(b,|\mathbf{W}|)}_{k|k}}} \tag{38d}$$

$$\mathcal{L}^{(j,\mathbf{W})}_k = \frac{(2\pi)^{\frac{|\mathbf{W}|d}{2}}2^{\frac{|\mathbf{W}|}{2}}}{|\mathbf{W}|^{\frac{d}{2}}}\frac{\left|V^{(j)}_{k|k-1}\right|^{\frac{v^{(j)}_{k|k-1}}{2}}}{\left|V^{(j,\mathbf{W})}_{k|k}\right|^{\frac{v^{(j,\mathbf{W})}_{k|k}}{2}}}\frac{\Gamma_d\left(\frac{v^{(j,\mathbf{W})}_{k|k}}{2}\right)}{\Gamma_d\left(\frac{v^{(j)}_{k|k-1}}{2}\right)} \times \frac{\left|\hat{X}^{(j)}_{k|k-1}\right|^{\frac{|\mathbf{W}|}{2}}}{\left|\hat{R}^{(j,\mathbf{W})}_{k|k-1}\right|^{\frac{|\mathbf{W}|-1}{2}}\left|S^{(j,\mathbf{W})}_{k|k-1}\right|^{\frac{1}{2}}} \times \frac{\Gamma\left(\alpha^{(j,|\mathbf{W}|)}_{k|k}\right)\left(\beta^{(j)}_{k|k-1}\right)^{\alpha^{(j)}_{k|k-1}}}{\Gamma\left(\alpha^{(j)}_{k|k-1}\right)\left(\beta^{(j,\mathbf{W})}_{k|k}\right)^{\alpha^{(j,|\mathbf{W}|)}_{k|k}}}. \tag{38e}$$

ACKNOWLEDGMENT

The authors would like to thank the LaMMA Consortium [51] for allowing the use of the exploited radar data. The research activity developed by the IREA group leading to this paper has been performed within the framework of the RITMARE Flagship Project, funded by the Italian Ministry of University and Research. The authors would also like to thank the anonymous reviewers for their valuable comments, which contributed to improve the quality of this paper.

REFERENCES

[1] E. Conte and M. Longo, "Characterisation of radar clutter as spherically invariant random process," *Proc. Inst. Elect. Eng.—F*, vol. 134, no. 2, pp. 191–197, Oct. 1987.

[2] E. Conte, M. Longo, and M. Lops, "Modeling and simulation of non-Rayleigh radar clutter," *Proc. Inst. Elect. Eng.—F*, vol. 138, no. 2, pp. 121–130, Apr. 1991.

[3] K. D. Ward, R. J. A. Tough, and S. Watts, *Sea Clutter: Scattering the K-Distribution and Radar Performance*. IET Radar, Sonar and Navigation Series 20. Hertz, U.K.: Inst. Eng. Technol., 2006.

[4] K. D. Ward, "Compound representation of high resolution sea clutter," *Electron. Lett.*, vol. 17, no. 16, pp. 561–563, Aug. 1981.

[5] S. Watts, C. J. Baker, and K. D. Ward, "Maritime surveillance radar. II. Detection performance prediction in sea clutter," *Proc. Inst. Elect. Eng.—F*, vol. 137, no. 2, pp. 63–72, Apr. 1990.

[6] A. Farina, F. Gini, M. V. Greco, and L. Verrazzani, "High resolution sea clutter data: Statistical analysis of recorded live data," *Proc. Inst. Elect. Eng.—Radar, Sonar Navigat.*, vol. 144, no. 3, pp. 121–130, Jun. 1997.

[7] Y. Bar-Shalom, P. K. Willett, and X. Tian, *Tracking and Data Fusion, A Handbook of Algorithms*. Storrs, CT, USA: YBS, 2011.

[8] S. Maresca, P. Braca, J. Horstmann, and R. Grasso, "Maritime surveillance using multiple high-frequency surface-wave radars," *IEEE Trans. Geosci. Remote Sens.*, vol. 52, no. 8, pp. 5056–5071, Aug. 2014.

[9] R. Mahler, *Statistical Multisource-Multitarget Information Fusion*. Norwood, MA, USA: Artech House, 2007.

[10] D. Daley and D. Vere Jones, *An Introduction to the Theory of Point Processes. Vol. 1, Elementary Theory and Methods*. New York, NY, USA: Springer-Verlag, 2003.

[11] P. Braca, S. Marano, V. Matta, and P. Willett, "Multitarget-multisensor ML and PHD: Some asymptotics," in *Proc. Int. Conf. Inf. Fusion*, Singapore, Jul. 2012, pp. 2347–2353.

[12] P. Braca, S. Marano, V. Matta, and P. Willett, "Asymptotic efficiency of the PHD in multitarget/multisensor estimation," *IEEE J. Sel. Topics Signal Process.*, vol. 7, no. 3, pp. 553–564, Jun. 2013.

[13] P. Braca, S. Marano, V. Matta, and P. Willett, "A linear complexity particle approach to the exact multi-sensor PHD," in *Proc. IEEE ICASSP*, Vancouver, BC, USA, May 2013, pp. 4061–4065.

[14] K. Granström, C. Lundquist, and U. Orguner, "Extended target tracking using a Gaussian mixture PHD filter," *IEEE Trans. Aerosp. Electron. Syst.*, vol. 48, no. 4, pp. 3268–3286, Oct. 2012.

[15] K. Gilholm and D. Salmond, "Spatial distribution model for tracking extended objects," *Proc. Inst. Elect. Eng.—Radar, Sonar Navigat.*, vol. 152, no. 5, pp. 364–371, Oct. 2005.

[16] K. Gilholm, S. Godsill, S. Maskell, and D. Salmond, "Poisson models for extended target and group tracking," in *Proc. SPIE, Signal Data Process. Small Targets*, Aug. 2005, vol. 5913 pp. 230–241.

[17] M. Beard, B. Vo, B.-N. Vo, and S. Arulampalam, "A partially uniform target birth model for Gaussian mixture PHD/CPHD filtering," *IEEE Trans. Aerosp. Electron. Syst.*, vol. 49, no. 4, pp. 2835–2844, Oct. 2013.

[18] J. W. Koch, "Bayesian approach to extended object and cluster tracking using random matrices," *IEEE Trans. Aerosp. Electron. Syst.*, vol. 44, no. 3, pp. 1042–1059, Jul. 2008.

[19] M. Feldmann, D. Fränken, and J. W. Koch, "Tracking of extended objects and group targets using random matrices," *IEEE Trans. Signal Process.*, vol. 59, no. 4, pp. 1409–1420, Apr. 2011.

[20] R. Mahler, "PHD filters for nonstandard targets, I: Extended targets," in *Proc. Int. Conf. Inf. Fusion*, Seattle, WA, USA, Jul. 2009, pp. 915–921.

[21] Marine Casualties Investigative Body, "Cruise Ship Costa Concordia, Marine casualty on January 13, 2012, Report on Safety Technical Investigation," Italian Ministry Infrastruct. Transp., Rome, Italy, Tech. Rep., 2013.

[22] K. Granström, C. Lundquist, and U. Orguner, "Tracking rectangular and elliptical extended targets using laser measurements," in *Proc. Int. Conf. Inf. Fusion*, Chicago, IL, USA, Jul. 2011, pp. 592–599.

[23] K. Granström and U. Orguner, "A PHD filter for tracking multiple extended targets using random matrices," *IEEE Trans. Signal Process.*, vol. 60, no. 11, pp. 5657–5671, Nov. 2012.

[24] S. Reuter and K. Dietmayer, "Pedestrian tracking using random finite sets," in *Proc. Int. Conf. Inf. Fusion*, Chicago, IL, USA, Jul. 2011, pp. 1101–1108.

[25] M. Wieneke and W. Koch, "A PMHT approach for extended objects and object groups," *IEEE Trans. Aerosp. Electron. Syst.*, vol. 48, no. 3, pp. 2349–2370, Jul. 2012.

[26] K. Granström, S. Reuter, D. Meissner, and A. Scheel, "A multiple model PHD approach to tracking of cars under an assumed rectangular shape," in *Proc. Int. Conf. Inf. Fusion*, Salamanca, Spain, Jul. 2014, pp. 1–8.

[27] A. Scheel, K. Granström, D. Meissner, S. Reuter, and K. Dietmayer, "Tracking and data segmentation using a GGIW filter with mixture clustering," in *Proc. Int. Conf. Inf. Fusion*, Salamanca, Spain, Jul. 2014, pp. 1–8.

[28] M. Baum and U. D. Hanebeck, "Shape tracking of extended objects and group targets with star-convex RHMs," in *Proc. Int. Conf. Inf. Fusion*, Chicago, IL, USA, Jul. 2011, pp. 338–345.

[29] S. Davey, M. Wieneke, and H. Vu, "Histogram-PMHT unfettered," *IEEE J. Sel. Topics Signal Process.*, vol. 7, no. 3, pp. 435–447, Jun. 2013.

[30] Y. Boers *et al.*, "A track before detect algorithm for tracking extended targets," *Proc. Inst. Elect. Eng.—Radar, Sonar Navigat.*, vol. 153, no. 4, pp. 345–351, Aug. 2006.

[31] B. Errasti-Alcala and P. Braca, "Track before detect algorithm for tracking extended targets applied to real-world data of X-band marine radar," in *Proc. Int. Conf. Inf. Fusion*, Salamanca, Spain, Jul. 2014, pp. 1–8.

[32] R. Mahler, "Multitarget Bayes filtering via first-order multi target moments," *IEEE Trans. Aerosp. Electron. Syst.*, vol. 39, no. 4, pp. 1152–1178, Oct. 2003.

[33] K. Granström, C. Lundquist, F. Gustafsson, and U. Orguner, "Random set methods: Estimation of multiple extended objects," *IEEE Robot. Autom. Mag.*, vol. 21, no. 2, pp. 73–82, Jun. 2014.

[34] A. K. Gupta and D. K. Nagar, *Matrix Variate Distributions*. Chapman and Hall, 2000, ser. Chapman and Hall/CRC Monographs and Surveys in Pure and Applied Mathematics.

[35] K. Granström and U. Orguner, "Estimation and maintenance of measurement rates for multiple extended target tracking," in *Proc. Int. Conf. Inf. Fusion*, Singapore, Jul. 2012, pp. 2170–2176.

[36] C. Lundquist, K. Granström, and U. Orguner, "An extended target PHD filter and a gamma Gaussian inverse Wishart implementation," *IEEE J. Sel. Topics Signal Process.*, vol. 7, no. 3, pp. 472–483, Jun. 2013.

[37] K. Granström and U. Orguner, "A new prediction update for extended target tracking with random matrices," *IEEE Trans. Aerosp. Electron. Syst.*, vol. 50, no. 2, pp. 1577–1589, Apr. 2014.

[38] Y. Bar-Shalom, X.-R. Li, and T. Kirubarajan, *Estimation with Applications to Tracking and Navigation*. New York, NY, USA: Wiley, 2001.

[39] B.-N. Vo, S. Singh, and A. Doucet, "Sequential Monte Carlo methods for multitarget filtering with random finite sets," *IEEE Trans. Aerosp. Electron. Syst.*, vol. 41, no. 4, pp. 1224–1245, Oct. 2005.

[40] B.-N. Vo and W.-K. Ma, "The Gaussian mixture probability hypothesis density filter," *IEEE Trans. Signal Process.*, vol. 54, no. 11, pp. 4091–4104, Nov. 2006.

[41] K. Granström and U. Orguner, "Implementation of the GIW-PHD Filter," Dept. Elect. Eng., Linköping Univ., Linköping, Sweden, Tech. Rep. LiTH-ISY-R-3046, Mar. 2012. [Online]. Available: http://urn.kb.se/resolve?urn=urn:nbn:se:liu:diva-94585

[42] K. Granström and U. Orguner, "On spawning and combination of extended/group targets modeled with random matrices," *IEEE Trans. Signal Process.*, vol. 61, no. 3, pp. 678–692, Feb. 2013.

[43] K. Granström, C. Lundquist, and U. Orguner, "A Gaussian mixture PHD filter for extended target tracking," in *Proc. Int. Conf. Inf. Fusion*, Edinburgh, U.K., Jul. 2010, pp. 1–8.

[44] K. Granström and U. Orguner, "On the reduction of Gaussian inverse Wishart mixtures," in *Proc. Int. Conf. Inf. Fusion*, Singapore, Jul. 2012, pp. 2162–2169.

[45] D. E. Clark, K. Panta, and B.-N. Vo, "The GM-PHD filter multiple target tracker," in *Proc. Int. Conf. Inf. Fusion*, Florence, Italy, Jul. 2006, pp. 1–8.

[46] K. Panta, D. Clark, and B.-N. Vo, "Data association and track management for the Gaussian mixture probability hypothesis density filter," *IEEE Trans. Aerosp. Electron. Syst.*, vol. 45, no. 3, pp. 1003–1016, Jul. 2009.

[47] J. Nieto Borge and C. Guedes Soares, "Analysis of directional wave fields using X-band navigation radar," *Coastal Eng.*, vol. 40, no. 4, pp. 375–391, Jul. 2000.

[48] G. Ludeno *et al.*, "X-band marine radar system for high-speed navigation purposes: A test case on a cruise ship," *IEEE Geosci. Remote Sens. Lett.*, vol. 11, no. 1, pp. 244–248, Jan. 2014.

[49] G. Ludeno, S. Flampouris, C. Lugni, F. Soldovieri, and F. Serafino, "A novel approach based on marine radar data analysis for high-resolution bathymetry map generation," *IEEE Geosci. Remote Sens. Lett.*, vol. 11, no. 1, pp. 234–238, Jan. 2014.

[50] G. Ludeno *et al.*, "Remocean system for the detection of the reflected waves from the Costa Concordia ship wreck," *IEEE J. Sel. Topics Appl. Earth Observ. Remote Sens.*, vol. 7, no. 7, pp. 3011–3018, Jul. 2014.

[51] "LaMMA Consortium: GeoPortal," accessed 04-December-2014. [Online]. Available: http://www.lamma.rete.toscana.it/en/geoportal

[52] "LaMMA Consortium: Wind measurements at the Giglio Island," accessed 04-December-2014. [Online]. Available: http://www.lamma.rete.toscana.it/node/3644

[53] "LaMMA Consortium: Archive of the Weather Reports," accessed 04-December-2014. [Online]. Available: http://www.lamma.rete.toscana.it/meteo/archivio-bollettini-meteo

[54] "LaMMA Consortium: Wind and Sea State Reference Scales," accessed 04-December-2014. [Online]. Available: http://www.lamma.rete.toscana.it/legenda-bollettino-mare-largo

[55] "LaMMA Consortium: Legend of Symbols," accessed 04-December-2014. [Online]. Available: http://www.lamma.rete.toscana.it/previ/ita/legenda.html

[56] M. Skolnik, *Introduction to Radar Systems*. New York, NY, USA: McGraw-Hill, 2002.

[57] N. Levanon, *Radar Principles*. Hoboken, NJ, USA: Wiley, 1988.

[58] N. Levanon and M. Shor, "Order statistics CFAR for Weibull background," *Proc. Inst. Elect. Eng.—F Radar Signal Process.*, vol. 137, no. 3, Jun. 1990, pp. 157–162.

[59] S. Kay, *Fundamentals of Statistical Signal Processing, Volume I: Estimation Theory*. Upper Saddle River, NJ, USA: Prentice-Hall, 1993.

[60] S. D. Dubey, "Some percentile estimators for Weibull parameters," *Technometrics*, vol. 9, no. 1, pp. 119–129, 1967.

[61] D. J. Sheskin, *Handbook of Parametric and Nonparametric Statistical Procedures*. London, U.K.: Chapman & Hall, 2011.

[62] P. Tait, *Introduction to Radar Target Recognition*, vol. 18. Herts, U.K.: Inst. Elect. Eng., 2006, ser. The IET Radar, Sonar, & Navigation Books.

Karl Granström (M'08) received the M.Sc. degree in applied physics and electrical engineering and the Ph.D. degree in automatic control from Linköping University, Linköping, Sweden, in 2008 and 2012, respectively.

He is a Postdoctoral Research Fellow with the Department of Electrical and Computer Engineering, University of Connecticut, Storrs, CT, USA. He previously held a postdoctoral position at the Department of Electrical Engineering of Linköping University from December 2012 to August 2014. His research interests include estimation theory, multiple model estimation, and sensor fusion and target tracking, particularly for extended targets.

Dr. Granström has received paper awards at the FUSION 2011 and FUSION 2012 conferences.

Antonio Natale (M'09) was born in Naples, Italy, on July 3, 1982. He received the B.S. and M.S. degrees (both *cum laude*) in telecommunication engineering from the University of Naples Federico II, Naples, in 2005 and 2008, respectively.

From December 2008 to January 2012, he was with the Electronic and Telecommunication Engineering Department of the University of Naples Federico II, where he got the Ph.D. degree. In 2011, he was a Visiting Scientist with the Surrey Space Centre of the University of Surrey, Guildford, U.K. In that period, he was also the Principal Researcher for the project "Applications for S-band SAR," funded by EADS Astrium Ltd. Since April 2012, he has been with the Istituto per il Rilevamento Elettromagnetico dell'Ambiente of the Italian National Research Council (CNR). In 2013, he spent a period at the NATO Centre for Maritime Research and Experimentation of La Spezia (Italy) as a Visiting Scientist to develop target detection and tracking strategies from high-resolution radar data. His research interests are in the field of remote sensing, with special regard to the modeling of electromagnetic scattering from natural surfaces, the signal processing, and the estimation of parameters from radar data.

Dr. Natale was awarded the IEEE Geoscience and Remote Sensing Society South-Italy Chapter prize in 2009, for the best Italian thesis in remote sensing discussed in 2008, and he was the recipient of the "2009 S. A. Schelkunoff Transactions Prize Paper Award" from the IEEE Antennas and Propagation Society, for the best paper published in 2008 in the IEEE TRANSACTIONS ON ANTENNAS AND PROPAGATION.

Paolo Braca (M'14) received the Laurea degree (*summa cum laude*) in electronic engineering and the Ph.D. degree (highest rank) in information engineering from the University of Salerno, Salerno, Italy, in 2006 and 2010, respectively.

In 2009, he was a Visiting Scholar with the Department of Electrical and Computer Engineering, University of Connecticut, Storrs, CT, USA, working with Prof. P. K. Willett. In 2010, he was a Senior Engineer with D'Appolonia S.p.A., Rome, Italy. In 2010 and 2011, he was a Postdoctoral Associate with the University of Salerno, Salerno, Italy. In October 2011, he joined the NATO Science and Technology Organization Centre for Maritime Research and Experimentation (CMRE, formerly known as SACLANTCENT and NURC) as a Scientist with the Research Department. He is involved in developing signal processing techniques for different kinds of sensor network technologies, including low-power radar sensor network (X-band and HF surface wave), sonar AUV network, and transponder-based satellite/terrestrial sensors. A special emphasis is given to the study of distributed and autonomous signal processing techniques applied to networked systems. Typically, these techniques are scientifically validated and tested during NATO experimentation in the field of maritime security and antisubmarine warfare. He is the coauthor of more than 70 publications in international scientific journals, conference proceedings, and NATO technical reports.

Dr. Braca is currently an Associate Editor of the IEEE SIGNAL PROCESSING MAGAZINE (E-Newsletter) and the *Journal of Advances in Information Fusion* and a reviewer for several scientific journals and conferences. He has been a Co-Organizer with Prof. P. K. Willett of the special session Multisensor Multitarget Tracking at the European Signal Processing Conference 2013. He was the recipient of the Best Student Paper Award (first runner-up) at the 12th Conference on Information Fusion in 2009.

Giovanni Ludeno (M'13) was born in Caserta, Italy, on January 28, 1984. In May 2011, he received the Master's degree in telecomunication engineering from the University Mediterranea of Reggio Calabria, Reggio Calabria, Italy.

From November 2011 to October 2012, he was in a scholarship with the Institute for Electromagnetic Sensing of the Environment (IREA), Naples, Italy, of the Italian National Research Council (CNR). From June 2012 to January 2015, he was with the Industrial and Information Engineering Department, Second University of Naples, Caserta, Italy, where he got the Ph.D. degree. From October 2012 to February 2014, he was a Research Fellow with the company Vitrociset SpA, dealing with the analysis of X-band radar data for the detection of reflective targets on the sea surface, carrying out this activity at the IREA-CNR in Naples. He is currently a Research Fellow with the IREA-CNR. His research interests concern the field of remote sensing with special regard to the development of innovative strategies for the estimation of sea state parameters, surface currents, and bathymetry through high-resolution nautical X-band radar data.

Francesco Serafino received the International Ph.D. degree in information and communication technologies in 2005 from the University of Naples Federico II, Naples, Italy, and in collaboration with DEOS Institute of Delft.

He spent more than ten years on synthetic aperture radar (SAR) data processing, differential SAR interferometry, and multipass 3-D and differential SAR tomography. At the moment, he is a Researcher at IREA-CNR of Naples, and his main scientific interest is focused on the extraction of hydrodynamic parameters from marine radar image sequences, with particular interest on the surface current and bathymetry map generation and space-time wave height reconstruction. He is the author of more than 50 papers and the inventor of two European patents. In September 2010, he founded a company, a spin-off of the CNR, REMOCEAN S.P.A., to commercialize a system for sea surface monitoring through the analysis of radar data. The company was judged in 2013 and 2014 among the top ten Italian start-ups.